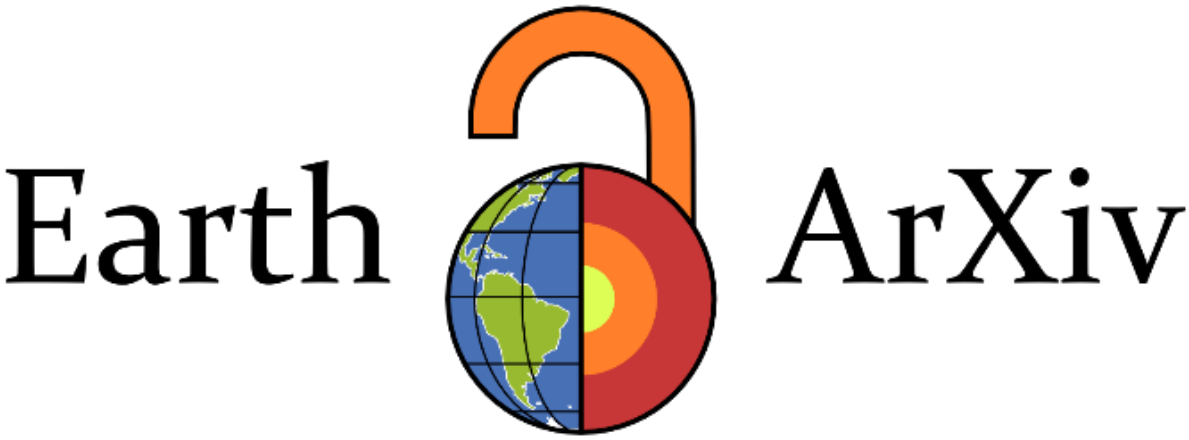

Alaskan Glacier Depths from a Decade of Airborne Radar Sounding

B. S. Tober[1,2], M. S. Christoffersen[3,4], J. W. Holt[1,4], M. Truffer[5,6], and C. F. Larsen[5]

[1]Dept. of Geosciences, University of Arizona, Tucson, AZ, USA

[2]Civil and Environmental Engineering, Carnegie Mellon University, Pittsburgh, PA, USA

[3]School of Earth and Atmospheric Sciences, Georgia Institute of Technology, Atlanta, GA, USA

[4]Lunar and Planetary Laboratory, University of Arizona, Tucson, AZ, USA

[5]Geophysical Institute, University of Alaska Fairbanks, Fairbanks, AK, USA

[6]Dept. of Physics, University of Alaska Fairbanks, Fairbanks, AK, USA

Corresponding author: Brandon S. Tober (btober@cmu.edu)

Key Points:

- Airborne radar proves capable of sounding through 1.5 km of temperate ice, mapping 5,600 linear-km of ice thickness across Alaska-Yukon
- Glacier termini across the region are overdeepened, which will lead to new and expanded proglacial lakes given continued melt and retreat
- Radar surface clutter remains the greatest challenge to resolving ice thickness for many of the region's unmapped glaciers

Abstract

NASA's Operation IceBridge employed airborne radar sounders in Alaska and adjacent northwestern Canada between 2012-2021 to measure the thickness of the region's glaciers. Here we present the first comprehensive analysis of these data, providing over 5,500 linear-km of ice thickness and bed elevation measurements – constituting the greatest ice thickness inventory for this region to date. Aside from glaciers of the Saint Elias Mountains, radar bed returns are limited to expansive accumulation areas and glacier termini, distant from sources of off-nadir surface topography. Gridded measurements across Bering Glacier reveal a subglacial trough extending over 50 km from the glacier's terminus up to the Bagley Ice Valley, likely a subglacial expression of the Bering Fault. We find that many of the glacier termini successfully sounded by Operation IceBridge have overdeepened beds, which may offer insight into the potential extent of proglacial lakes and associated natural hazards given continued thinning and retreat. While the long-wavelength sounders employed by Operation IceBridge have proven capable of sounding through nearly 1500 m of temperate ice, radar surface returns from the flanks of the region's mountain glaciers remain the greatest challenge to identifying glacier bed returns and retrieving ice thickness measurements. Simulating these returns in the survey planning may significantly improve the mapping success of future airborne radar campaigns.

Plain Language Summary

NASA's Operation IceBridge conducted airborne radar surveys in Alaska and northwestern Canada from 2012 to 2021. This study presents over 5,500 linear-km of ice thickness and bed elevation measurements from these surveys—the most extensive inventory of such measurements to date for the region. IceBridge radar sounding reveals that the termini of many glaciers across the region have deep basins beneath them, which may influence the formation of lakes and associated hazards as these glaciers thin and retreat. Although airborne radar sounding has effectively probed through ice up to 1,500 m thick, the region's unmapped valley glaciers remain difficult targets due to radar reflections from the surrounding topography.

1 Introduction

Globally, runoff from glacial melt contributes around 250 Gt yr^{-1}, or around 1 mm yr^{-1} to eustatic sea level rise (Jacob et al., 2012; Gardner et al., 2013), with up to ~150 mm of additional sea level rise from glacial melt expected by the end of the century (Rounce et al., 2023). Glaciers in Alaska and adjacent northwestern Canada (Yukon and northern British Columbia; hereafter referred to collectively as "Alaska") led global glacial melting during the latter half of the 20th century (Arendt et al., 2002), and remain the leading glacial contributor to global sea level rise today at up to 75 Gt yr^{-1} (Arendt et al., 2013; Larsen et al., 2015; Harig & Simons, 2016; Zemp et al., 2019; Hugonnet et al., 2021). The latest estimates indicate that aside from Earth's two ice sheets, Alaska will remain the greatest regional contributor to global sea level rise through the end of the year 2100, reaching between 0.33 and 0.44 mm sea level equivalent per year by mid-century (Rounce et al., 2023).

Local and regional impacts of rapid deglaciation include the opening of previously ice-filled fjords (Post et al., 2011; Carlson et al., 2017), the formation of new proglacial lakes

(Larsen et al., 2007; Field et al., 2021), glacial lake outburst floods (Kienholz et al., 2020), and abrupt watershed reorganization (Shugar et al., 2017). Continued landscape change is expected in the wake of glacial retreat, including the abandonment and rerouting of established river channels (Loso et al., 2021). Changes in the timing and magnitude of glacial runoff (Huss & Hock, 2018; Young et al., 2021) also hold implications for downstream water users.

Despite Alaska's large contribution to sea level rise, precise mass loss projections and our understanding of the evolution of the region's glaciers and the landscape they occupy remain limited largely due to uncertainty in regional ice volumes (Millan et al., 2022; Rounce et al., 2023). While individual glacier surface areas are readily available (Pfeffer et al., 2014), the sparsity of ice thickness measurements leads to significant uncertainty in glacier volumes. Efforts to model glacier volumes globally (Farinotti et al., 2019; Millan et al., 2022) can be riddled with large errors for individual glaciers (Bahr et al., 2015). Tober et al. (2023) demonstrated that such models overestimate the volume of Malaspina Glacier – one of Alaska's largest ice masses – by at least 30%. Errors in the estimation of ice thickness for Malaspina are likely exacerbated by the glacier's surge-type nature (Post, 1969), which may indicate that many of the other surge-type glaciers in Alaska have large volume errors in global ice thickness models as well. Still, non-surge type glaciers are also hampered by ice thickness modeling errors (e.g. Taku Glacier; Borthwick et al., 2025).

Owing to the transparency of glacial ice at radio frequencies, radar sounding has become a ubiquitous approach to providing measurements of ice thickness and subglacial topography (Bogorodsky et al., 1985), probing through several kilometers of ice over Earth's two polar ice sheets (Gogineni et al., 1998), and even on Mars (Plaut et al., 2007). However, in comparison to polar ice, temperate glaciers such as those found in Alaska (Molnia, 2001) provide a more challenging target due to multiple factors, including scattering of incident radio waves in the presence of water-filled englacial cavities (Smith & Evans, 1972) and greater attenuation of radar energy due to the higher ice temperatures (MacGregor et al., 2007). Mountain glaciers across Alaska also host an abundance of supraglacial debris (Scherler et al., 2018; Herreid & Pellicciotti, 2020) and often have highly crevassed surfaces, causing a portion of incident radio waves to be scattered at the glacier surface. Radar frequencies of $\leq$10 MHz are generally required to successfully combat these losses and probe temperate ice masses (Watts & England, 1976). Airborne sounding efforts in Alaska have demonstrated that optimal frequencies are between 1 and 5 MHz (Conway et al., 2009; Rignot et al., 2013; Tober et al., 2023). Between 2012 and 2021, several airborne radar sounders with center frequencies ranging from 2.5 to 5 MHz were employed in Alaska through NASA's Operation IceBridge (MacGregor et al., 2021). Investigation of this dataset provides the most extensive inventory of Alaskan ice thickness measurements to date (Figure 1).

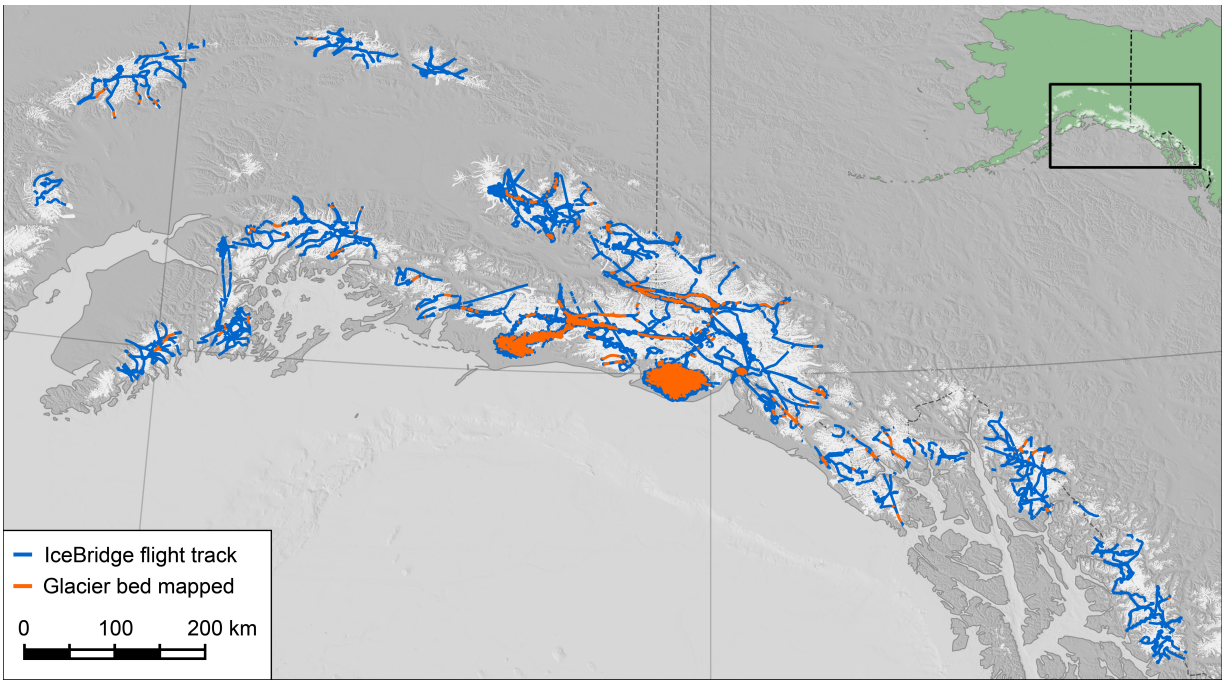

Figure 1. Study area overview map showing 2013-2021 Operation IceBridge radar sounding flight tracks in blue, and along-profile locations where ice thickness and bed topography measurements were obtained in orange.

2 Data and Methodology

Long-wavelength radar sounders developed for use by Operation IceBridge in Alaska include the Warm Ice Sounder Experiment (WISE; Rignot et al., 2013), the University of Alaska Fairbanks High-Frequency system (UAFHF; Truffer et al., 2021), and the Arizona Radio Echo Sounder (ARES; Holt et al., 2021). Overall properties of each of these systems are outlined in (MacGregor et al., 2021).

Data from the Warm Ice Sounder Experiment acquired during the 2012 IceBridge campaign are described by Rignot et al. (2013). Enderlin et al. (2016) note that results presented in Rignot et al. (2013) and subsequently submitted to the Glacier Thickness Dataset (GlaThiDa; Welty et al., 2020) are erroneous, as the authors did not perform an analysis to verify that interpreted bed echoes were not off-nadir surface returns ("surface clutter"), a process described by Holt et al. (2006) for such environments. Proper validation of the measurements presented by Rignot et al. (2013) would compare radar profiles against clutter simulations, as was performed in this study for all UAFHF and ARES radar profiles (Section 2.1). However, as only the derived measurements of ice thickness and bed elevation - and not the radar data itself - are publicly available, we are unable to perform such validation for the WISE data. We therefore limit our investigation of Operation IceBridge-Alaska airborne radar sounding to data acquired by UAFHF and ARES, which were operated between 2013-2021.

2.1 IceBridge radar processing and interpretation

A standardized signal processing routine was developed and applied to all UAFHF and ARES radar profiles. Linear frequency modulated data (ARES) were pulse-compressed, using a boxcar-windowed reference waveform as a matched filter. Radar profiles were coherently summed in the slow-time direction by a factor of 100, increasing the signal to noise ratio by a factor of 10. The mean trace was subtracted from each profile along a rolling window. Following signal processing, all 31,700 linear-km of radar profiles acquired in Alaska between 2013 and 2021 were investigated for the presence of glacier bed returns. Radar returns from off-nadir topography ("surface clutter") were modeled and compared to each radar profile to confirm that any suspected bed returns were not surface clutter (Holt et al., 2006). Once radar returns were confidently qualified as glacier bed returns, they were manually digitized ("picked") along radar profiles using the Radar Analysis Graphical Utility (Tober & Christoffersen, 2020). For impulse radar data (UAFHF), glacier bed returns were picked as the leading edge ("first-break"), while for pulse-compressed linear frequency modulated data (ARES), peak amplitudes were picked.

Digitized glacier bed returns provide point measurements of the two-way travel time from the radar sounder to the glacier's bed. The position assigned to each point-measurement was taken as the Precise Point Positioning solution to the location of the survey aircraft using a GPS antenna mounted atop the aircraft. The ground spacing of point measurements is dependent on the radar pulse repetition frequency (typically 1 or 2 kHz), the aircraft ground speed (usually around 50 m s^{-1}), as well as coherent summing in post-processing, resulting in a median along-track spacing of 3 m for ARES data and 60 m for UAFHF data. Flight parameters were primarily constrained by the laser altimeter and science priorities of Operation IceBridge, requiring flight altitudes of 300 – 500 m above the surface (above-ground-level, AGL) and repeats of previous flight tracks, typically along centerline profiles. For ARES data, the transmit

pulse length was typically 3 or 5 µs, so the sounder was still transmitting at the time of the surface return, rendering the surface indiscernible in most cases (e.g. Figure 2).

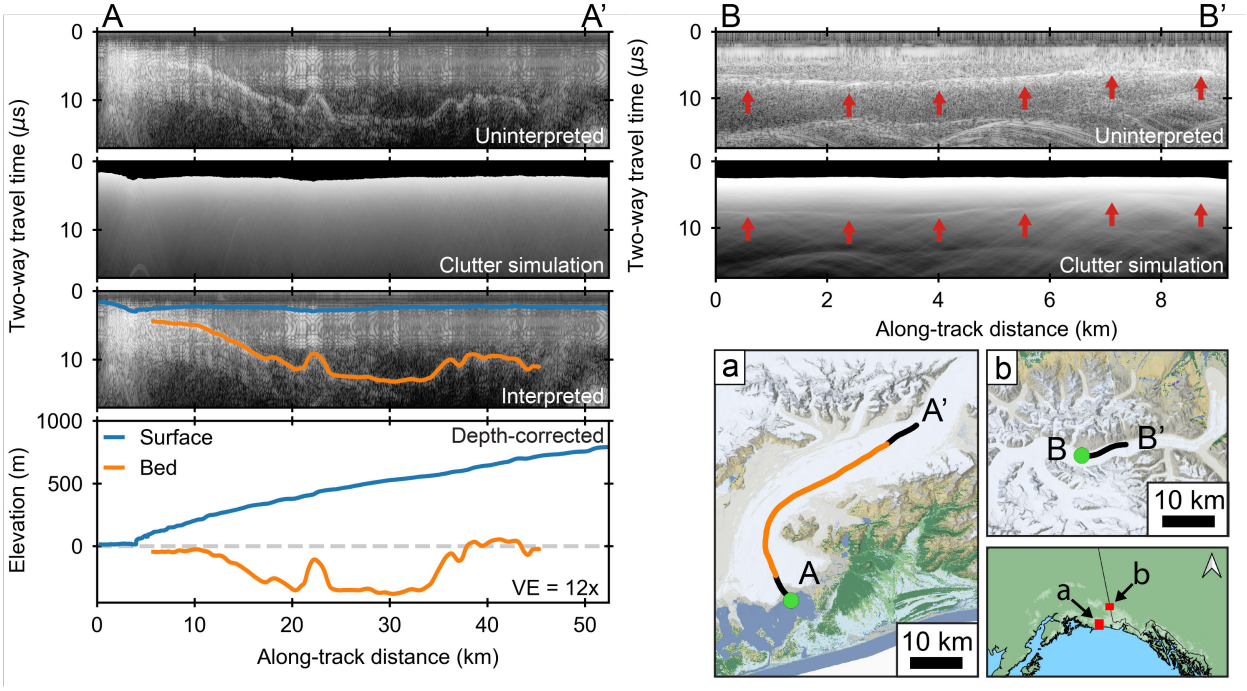

Figure 2. ARES longitudinal radar profile examples over Bering Glacier, AK (A-A') and Klutlan Glacier, AK/Yukon Canada (B-B'). The upper panel for both radar profiles shows the uninterpreted radar data, while the second panel down shows the corresponding clutter simulation. For Bering profile A-A', the third panel down shows the interpreted radar profile with the lidar-derived surface in blue and the manually digitized bed in orange, and the bottom panel shows the depth-corrected elevation profile. For Klutlan profile B-B', red arrows in the upper panel point to a radar return that mimics an expected bed return but can be confirmed as off-nadir surface clutter in the second panel down. Location insets shown at bottom right, with map-view location of Bering profile A-A' shown in panel (a), and Klutlan profile B-B' shown in panel (b) Orange line segment in (a) corresponds to the location of bed picks made for profile A-A'.

Measurements of the surface elevation coincident with radar measurements of travel time to the glacier's bed are necessary to derive englacial travel time delays and thereby ice thickness. For ARES data where the reflection from the glacier surface is obscured by the outgoing signal, we calculate the glacier surface height from the lidar point cloud as the median height of all points within the first Fresnel zone of the radar (typically 200 to ~350 m in diameter), assuming this captures the centroid position from which radar returns originate (Text S1). The median elevation value was chosen to avoid negatively skewing the derived surface elevation in the presence of crevasses. Laser altimetry data were not available for several radar profiles acquired in 2021. For those profiles the surface elevations were derived from the Center for Remote Sensing of Ice Sheets (CReSIS) snow radar (Paden et al., 2014; Rodriguez-Morales et al., 2014), which was present for those flights, using the same

methodology of taking the median surface elevation value from all snow radar soundings within the first Fresnel zone of each ARES sounding.

Radar travel times in ice were derived by subtracting the calculated travel times in air from the total radar-derived travel time to the glacier bed. Converting englacial travel times to depth requires knowledge of the radio wavespeed in ice $v = c/\sqrt{\varepsilon'}$, where c is the wavespeed in a vacuum and ε' is the real part of the dielectric permittivity (dielectric constant). At typical radar sounding frequencies (on the order of 1 MHz), laboratory studies have shown that the dielectric constant of ice is between 3.1 and 3.2 (Evans, 1965; Fujita et al., 2000). Englacial travel time delays were converted to ice thickness assuming a dielectric constant of 3.15 (wavespeed of 169 m μs^{-1}), and the associated ± 1 m μs^{-1} uncertainty in wavespeed was propagated to the uncertainty in derived thicknesses. After converting englacial time delays to depth, subglacial elevation was determined by subtracting ice thickness from the surface elevation, and is reported as height in reference to the WGS84 ellipsoid.

2.2 Radar measurement uncertainties

The theoretical range (vertical) resolutions in ice for the radar sounders included in this study are 17 m for UAFHF (1/4 wavelength following Rayleigh's criterion), and 34 m at 2.5 MHz, or 17 m at 5 MHz for ARES, respectively (wavespeed divided by twice the transmitted waveform's bandwidth). While this system property is often discussed in terms of the measurement uncertainty for a given sounder, in reality it represents the ability to distinguish two signals close in time delay. As we are only concerned with echoes from the glacier bed, the range resolution is not entirely representative of our measurement uncertainty. To properly quantify the vertical uncertainty in radar-derived measurements of ice thickness and bed elevation, we compared measurements derived from several interpreters, and also assessed the disagreement of intersecting radar profiles (Lapazaran et al., 2016). Measurement uncertainty is also impacted by the horizontal resolution of glacier bed echoes, which can be considered similarly to the horizontal resolution at the glacier surface given by the first Fresnel zone (Sheriff, 1980; Text S1). We numerically assess the horizontal resolution at the bed by determining the near-nadir area from which plane waves will be reflected to the sounder with a separation distance of less than half a wavelength, following refraction at the air-ice interface and a change in the electromagnetic wavespeed (Text S2). For a typical operational altitude of 300 m and an ice thickness range of 100 to 1000 m, the horizontal resolution at the glacier's bed ranges from approximately 150 to 230 m at a radar center frequency of 2.5 MHz, and from 100 to 160 m at 5 MHz, with the resolution degrades with distance from the sounder to the glacier's bed.

As no lever-arm correction was applied to account for the offset between the GPS antenna and the phase center of the radar antenna (Section 2.1) there is additional horizontal uncertainty in radar-point measurements. The exact phase center of each antenna is not

precisely known but is expected to be somewhere within the leading half of the antenna, or up to 15 m behind the aircraft for ARES data, and up to 60 m behind the aircraft for UAFHF data.

3 Results

3.1 Alaskan mountain glacier thickness inventory

Between 2013 and 2021, Operation IceBridge flew and acquired radar profiles over 591 glaciers in Alaska (using Randolph Glacier Inventory version 6, "RGI," outlines; RGI Consortium, 2017), with the combined profile distance totaling up to nearly 31,700 linear-km. Investigation of this dataset provides measurements of ice thickness and subglacial elevation across 5,600 linear-km, over 88 glaciers (Figures 1, S1-S9, Table S1). For these 88 glaciers, the median cumulative profile distance of bed detections is 11 linear-km. The majority of the achieved measurements are from the extensive glaciated terrain at the corner of southern Alaska. When combining the 2,000 linear-km of measurements presented by Tober et al. (2023) for the Malaspina piedmont glacier with measurements from Bering Glacier, Steller Glacier, Tana Glacier, and the Bagley Ice Valley, we obtain 4,011 linear-km of radar sounding measurements across the world's largest nonpolar ice complex (Windnagel et al., 2022).

Measurements were obtained across Bering Glacier and the piedmont lobe of Malaspina Glacier along radar profiles that are generally spaced between 2 and 3 km apart (Figure S4). As with the Malaspina piedmont lobe, nearly the entire piedmont lobe of Bering Glacier rests below sea level (median bed elevation of -120 m, median thickness of 365 m). Radar profiles show several subglacial troughs, where bed elevation generally extends to more than 350 m below sea level, reaching 470 m below sea level near the glacier's terminus. These troughs are apparent across all radar profiles transverse to the glacier's flow, indicating a continuous subglacial trough that extends to the Bagley Ice Valley, where bed elevation remains more than 250 m below sea level and ice thickness in excess of 1000 m is measured.

Other particularly well-mapped glaciers include the main trunks of Walsh Glacier (155 linear-km mapped), and Logan Glacier (125 linear-km mapped), with ice as thick as 1100 m found at Logan (Figure S5). For many of the other glaciers mapped by IceBridge, measurements are limited primarily to the terminus and accumulation areas (e.g. Columbia, Miles, Nabesna, Kennicott, Hubbard, and Tweedsmuir glaciers). IceBridge radar sounding reveals that the

termini of numerous glaciers across the region are overdeepened, with bed elevation decreasing in the up-glacier direction (Figure 3).

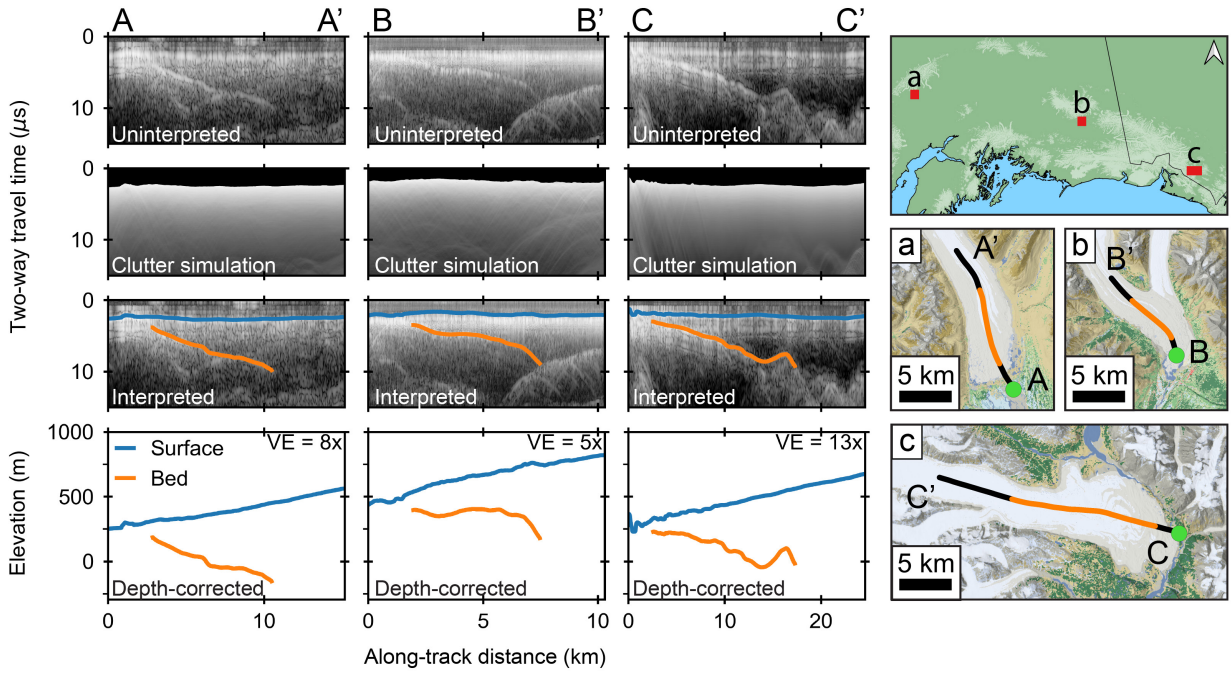

Figure 3. Examples IceBridge radar sounding profiles for glaciers exhibiting overdeepened termini. Profile A-A' shows Kahiltna Glacier, profile B-B' shows Kennicott Glacier, and profile C-C' shows Tweedsmuir Glacier. Map view location of profiles A-A', B-B', and C-C' are shown in panels (a), (b), and (c), respectively. Orange line segments indicate locations of bed picks in corresponding radar profiles

3.2 Measurement uncertainty

Interpretations of ice thickness were compared between various interpreters to assess measurement uncertainty as a function of interpretation bias. Randomly selected radar profiles were independently interpreted by two people for each radar sounder operated during each IceBridge campaign (N=20 profiles). This analysis demonstrated a median (and interquartile range) difference in ice thickness of 5 (8) m for UAFHF data, and 17 (12) m for ARES. Measurement uncertainty was more robustly assessed through crossover analysis. Ice thickness and bed elevations were independently compared at the 1,829 profile intersections where measurements were achieved (Figure S10). The median (and interquartile range) disagreement in ice thickness is 18 (24) m, while that of bed elevation is 15 (21) m. The results of this crossover analysis are nearly identical when only comparing measurements at profile intersections from the same radar system. We note that some disagreement in ice thickness may be explained by glacier thinning or thickening during the temporal span of this dataset (<=8 years), and that some disagreement in bed elevation may similarly be explained by bedrock erosion. However, while glaciers are thinning at an average rate of ~1 m yr^{-1} at the regional scale (Larsen et al., 2015) and localized erosion rates are as high as 3 m yr^{-1} (Motyka et

al., 2006), we observe no correlation between the disagreement in either ice thickness or bed elevation and the time span between profile crossings.

We uniformly applied a dielectric constant of 3.15 to convert englacial radar travel time delays to ice thickness, while assessing errors associated with the bulk wavespeed uncertainty. Assuming an uncertainty in the bulk dielectric constant of ± .05 (wavespeed range of 168 – 170 m μs^{-1}) gives an ice thickness uncertainty of 2%, which corresponds to ±8 m and ±23 m for the median and the maximum ice thickness measurements presented herein, respectively. Potential wavespeed-associated thickness uncertainty also arises from our assumption of a constant vertical density. Firn depths atop temperate glaciers in Alaska can reach up to 30 m, with a depth-dependent density structure (Arcone, 2009). The dielectric constant of firn varies as a function of density and liquid water content. For polar firn, the dielectric constant can range between approximately 2 and 3.15 (Kovacs et al., 1995; Arcone, 2009). Temperate firn, on the other hand, may have a higher dielectric constant. An analysis of radar sounding data across the Bagley Ice Valley gave an average value of 6.3 for the dielectric constant of the firn layer (Arcone, 2002). Applying too low a dielectric constant (too high a wavespeed) in our depth conversion leads to an overestimate of the firn layer thickness, while applying too high a dielectric constant leads to an underestimate ($\sqrt{\varepsilon'_{firn}/\varepsilon'_{ice}}$). Regardless of the uncertainty in the dielectric constant of overlying firn, if we consider a 30-m-thick firn layer atop ~1000 m of ice, the resulting uncertainty in the total column thickness for a range in the dielectric constant between 2 and 6.3 is less than 1.5% of the total thickness. Similarly, the potential presence of englacial liquid water, as observed by Bradford & Harper (2005) at Bench Glacier, Alaska, would introduce heterogeneity in the true englacial wavespeed, leading to errors in the derived ice thickness.

3.3 Subglacial topography of the Bering Glacier System

Given the radar-derived measurement density across Bering Glacier, the central Bagley Ice Valley, and the main branch of Tana Glacier, point-measurements of bed elevation were gridded through Gaussian process regression (Rasmussen & Williams, 2006), following the methods of Tober et al. (2023). Bed elevation inferences were made across a uniform grid with a spatial resolution of 100 m, conditioned upon radar-derived measurements as well as surface elevations provided by the Copernicus global 30 m spatial resolution (henceforth referred to as Copernicus-30) digital elevation model along the ice boundary, resulting in a probability distribution over continuous bed elevations, $P(\hat{b})$.

Randomly sampling from the resulting distribution of bed solutions, we find that south of the Bagley Ice Valley between 550 – 635 km^2, or 35 – 40%, of Bering Glacier (and nearly the entire piedmont lobe) is grounded below sea level (Figure 4). Two prominent troughs cut the bed of the piedmont, along which bed elevation reaches 450 m below sea level. These troughs appear to merge near the head of the piedmont and continue as a single trough up the entire length of the glacier (~55 km) to the divide between the east and west branches of the Bagley Ice Valley (Figure 4a). At this divide between the Bering, Steller, and Tana glaciers, bed

elevation reaches a local minimum of 300 m below sea level, and ice thickness reaches a maximum of 1370 m. Approximately 20 km to the east of this divide, ice thickness reaches 1480 m (Figure 4b).

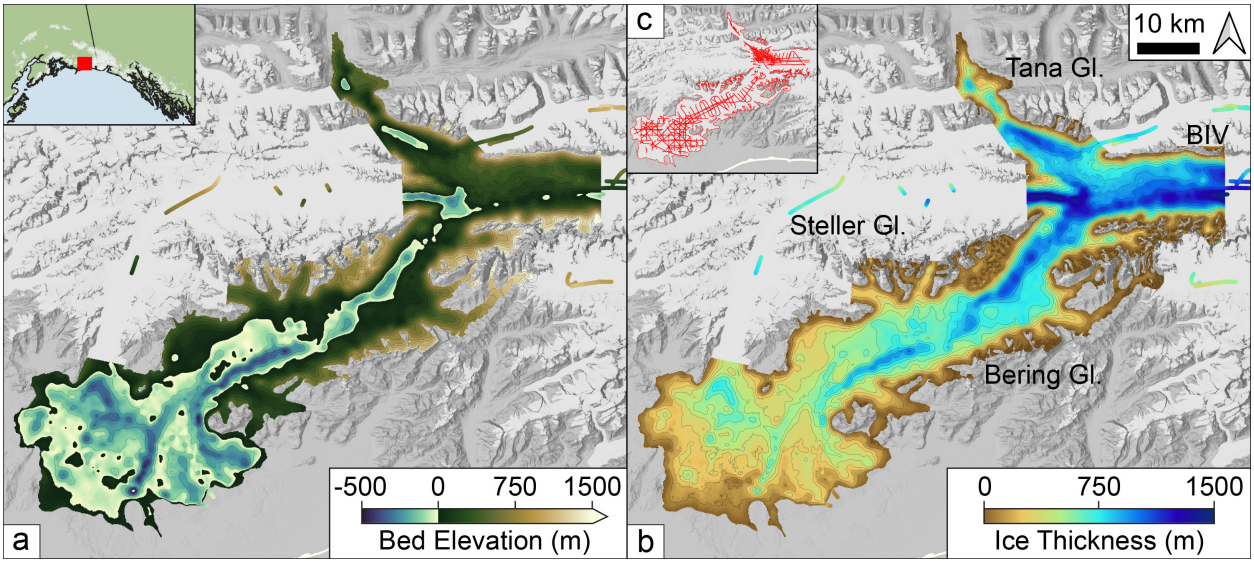

Figure 4. Bed elevation and ice thickness for the Bering Glacier system. IceBridge radar-derived along-profile and gridded (a) bed elevation, and (b) ice thickness. (c) Along-profile IceBridge measurement and visible ice boundary (from RGI outlines) locations which served as model training data shown in red. Location inset map at upper left corner of panel (a). Bagley Ice Valley is denoted as "BIV."

The median and interquartile range uncertainty in gridded bed elevation across Bering Glacier are 12 and 76 m. Subtracting the gridded bed elevation from the 2011 Copernicus-30 digital elevation model, we find that on average Bering Glacier is more than 500-m-thick (Figure 4b). Ice thickness increases to more than 800 m atop observed basal troughs.

4 Discussion

4.1 Retrograde glacier beds lead to the expansion of proglacial lakes

The expanse of proglacial lakes has been well-documented globally (e.g. Otto, 2019) and regionally (e.g. Field et al., 2021). Pronounced erosion during glacial advance cycles systematically forms depressions, which may result in subglacial topography that deepens in the up-glacier direction ("retrograde bed" or "overdeepening"). As mountain glaciers retreat since the Little Ice Age, these overdeepenings may be exposed and trap glacial meltwater along the glacier's frontal margin. IceBridge radar sounding data provide insight into the potential continued expanse of proglacial lakes across Alaska. We observe notable retrograde beds for a number of glaciers, including Kahiltna, Ruth, Kennicott, Nizina, Nabesna, Tana, Bering, Malaspina, Tweedsmuir, and Taku (e.g. Figs 2, 3). The expanse of proglacial lakes is apparent over the timespan of Landsat observations for a number of these systems (Field et al., 2021),

and radar sounding shows that for many Alaskan glaciers, their proglacial lakes will expand well beyond their current sizes with future retreat.

Larsen et al. (2015) showed significant mass loss signals over lake-terminating glaciers. Although some studies have found that calving is not the dominant mass loss mechanism (Boyce et al., 2007; Trüssel et al., 2015), other feedbacks can contribute substantially. Unlike glaciers that retreat upslope and lose their low-lying ablation area—reducing melt through a negative feedback (Jóhannesson et al., 1989; Harrison et al., 2003)—lake-terminating glaciers often retain their ablation areas where melting is greatest. Truffer & Motyka (2016) speculated that this continued exposure to high ablation rates explains their high mass loss rates. In extreme cases, such as the Yakutat Icefield, the entire glacier may be subject to such an instability (Trüssel et al., 2015). Our measurements are critical in assessing whether glacier evolution will be dominated by the positive mass balance - elevation feedback, or the negative feedback resulting from upslope glacier retreat (Harrison et al., 2003).

Proglacial lakes are sometimes dammed by a former terminal moraine and composed of loose, erodible material, and can thus pose a significant natural hazard to downstream infrastructure and ecosystems due to the potential for catastrophic outburst floods. The continued growth of proglacial lakes increases this risk (Lützow et al., 2024).

4.2 Ice-obscured tectonic structure of the Saint Elias Ice Complex

Bering Glacier is positioned at a structural boundary at the western extent of the Yakutat terrane, which is obliquely converging with the North American plate at a rate of ~50 mm yr^{-1} (Bruhn et al., 2004; Plafker, 1987), producing the pronounced topography of the Saint Elias orogen. East of Bering Glacier, folds and faults of the Saint Elias orogen mainly trend W to WSW, curving to strike N to NE towards the Aleutian subduction zone near the piedmont lobe of Bering Glacier (Bruhn et al., 2010, 2012). This tectonic boundary beneath the Bering Glacier is inferred to be a thrust or oblique-slip thrust fault projecting onshore from the Aleutian megathrust, and concealed by ice cover (Bruhn et al., 2012). Asymmetric troughs beneath the western half of Malaspina Glacier are suspected to be subglacial expressions of faults extending onshore from the Pamplona zone, the active deformation zone from of the Yakutat terrane (Tober et al., 2023). We suspect that the distinct basal trough observed extending beneath Bering Glacier up to the Bagley Ice Valley is also connected to the region's tectonic structure. Bruhn et al. (2012) mapped a thrust fault (possibly with oblique-slip) running along Bering Glacier ("Bering fault") that matches the approximate location of the trough we observe beneath the glacier (Figure 5). There is also a distinct asymmetry in the geometry of the Bagley Ice Valley, with a subglacial trough running parallel and proximal to the southern valley wall (profile D-D' of Figure 5), likely an expression of the Bagley fault zone. Fault zone fractures and relative weakness may allow for preferential glacial erosion along the faults of this glaciated

terrain. Radar sounding has therefore helped to reveal tectonic structure of the Saint Elias orogen which has until now remained concealed by ice cover.

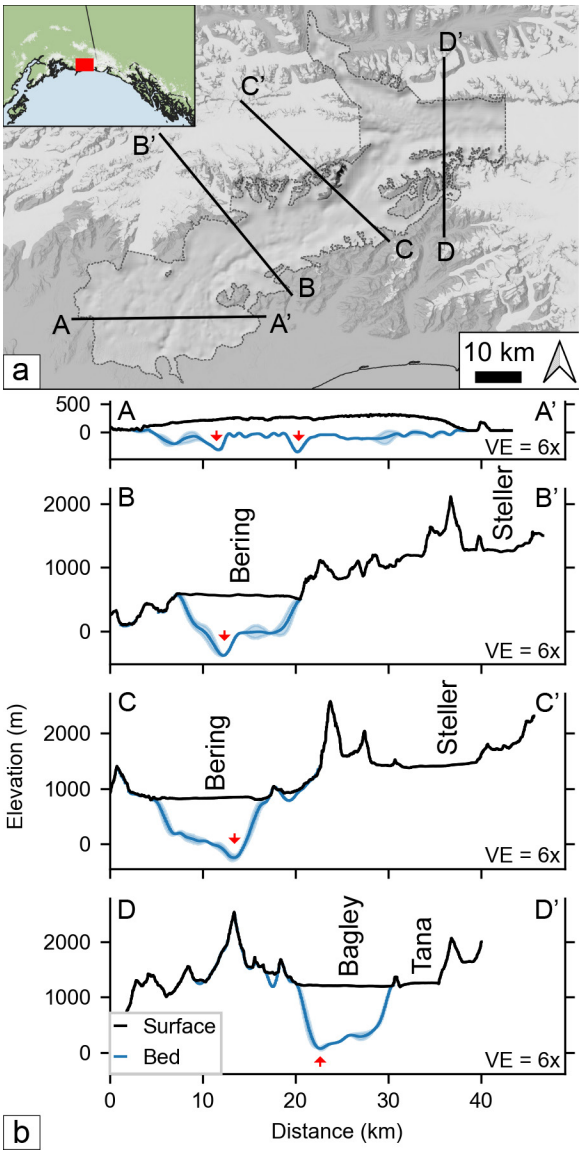

Figure 5. Geometries of Bering Glacier and the Bagley Ice Valley. (a) Hillshaded regional surface topography with RGI glaciated areas in white, overlain by hillshaded bed elevation model of the Bering Glacier system outlined by dotted black line. (b) Elevation profiles across Bering Glacier's piedmont lobe (A–A'), farther up-glacier (B–B', C-C'), and across the central Bagley Ice Valley (D–D'). Red arrows indicate subglacial troughs likely associated with regional tectonic structures.

4.3 Comparison with global ice thickness models

Comparing the ice thicknesses from gridded radar observations across the Bering Glacier system (including parts of Tana Glacier and the Bagley Ice Valley; Figure 4b) with global ice

thickness models, we find a mean absolute error of 240 m for the estimates by Farinotti et al. (2019) and a mean absolute error of 145 m for those by Millan et al. (2022; Figure 6). Similar to results shown by Tober et al. (2023) for Malaspina Glacier, the bed elevation of Bering Glacier obtained by subtracting the ice thickness models of Farinotti et al. (2019) and Millan et al. (2022) from the Copernicus-30 digital elevation model also differ significantly from the gridded bed elevation model presented herein (Figure S12). While both global models show large areas of the glacier grounded below sea level (nearly the entire glacial system for Farinotti et al. (2019), neither capture the clear structural patterns demonstrated by radar measurements. The glacier's true basal morphology, which is not captured by these models, is critical to the routing of subglacial drainage and the glacier's future evolution.

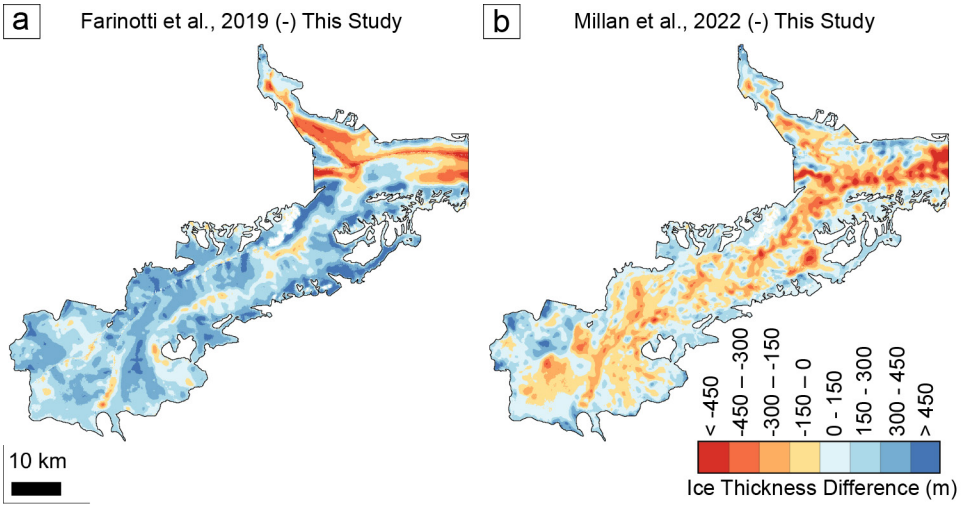

Figure 6. Difference in ice thickness obtained by subtracting that presented for the focus area of this study from the ice thickness presented by (a) Farinotti et al. (2019) and from the ice thickness presented by (b) Millan et al. (2022). Cool colors indicate overestimation of ice thickness by global models, while warm colors indicate an underestimation.

4.4 Implications for planning future airborne radar surveys

The legacy of Operation IceBridge-Alaska provides valuable insight on the sounding of temperate glaciers which we suspect is also applicable to other regions. The evolution of long-wavelength radar sounders deployed in Alaska have proven capable of probing temperate ice up to ~1500-m-thick within the Bagley Ice Valley, which to our knowledge is the greatest temperate ice thickness measurement provided by an airborne sounder to date.

We note that Operation IceBridge was a laser altimetry focused mission, with surveys typically repeating previous flightlines to map changes in surface elevation. These flightlines were often oriented sub-optimally for airborne radar sounding, either at too high an altitude above the glacier's surface, or too close to adjacent valley walls. Except for glaciers of the Saint Elias Ice Complex (Bering Glacier, the Bagley Ice Valley, and Malaspina Glacier), measurements of ice thickness and bed elevation are primarily limited to glacier termini and expansive accumulation areas. Valley glaciers remain the most challenging targets for radar sounding in

Alaska – not due to the depths of their temperate ice, but due to the occurrence of significant radar surface clutter produced by the surrounding valley walls from the use of non-directional radar antennas. While we simulate these topographic surface returns to ensure that suspected glacier bed returns are not in fact surface clutter, future radar survey planning should explicitly consider the expected time delay of off-nadir surface returns to increase the likelihood of obtaining discernible glacier bed returns.

Many of Alaska's alpine glaciers are located within valleys ranging between roughly 2 and 4 km in width. At the center of such valleys, the two-way travel time delay of radar returns from the adjacent valley walls is thus between 6.5 and 13.5 µs. In practice, we find that glacier bed returns must generally precede valley wall returns by a minimum two-way travel time delay of ~1 µs to be picked with confidence. With this knowledge, and an expected range of ice thickness, airborne radar surveys can be planned to maximize interpretability of glacier bed returns and avoid interference from off-nadir surface clutter. The suggested flight altitude above the glacier surface z can be generalized as:

$$z \leq \frac{v_1}{2}\left(\frac{w}{v_1} - \frac{2h}{v_2} - 1\,\mu s\right) \quad (1)$$

where w is the valley width in meters, or twice the distance from the adjacent valley wall, v_{air} is the radio wavespeed in air and v_{ice} is the radio wavespeed in ice, both in m µs^{-1} (Text S3). For instance, in a 3-km-wide valley, flying at 600 m AGL, it is possible to resolve ice thicknesses up to 600 m. Reducing the flight altitude to 400 m AGL improves this to 700 m (Figure 7). This insight also explains the lack of success in airborne sounding of Ruth Glacier's "Great Gorge." The 600-950 m depths estimated by Tober et al. (2024) through mass conservation within the ~2 km glacial valley indicate that off-nadir, valley-wall returns would always precede subglacial bed returns from an airborne radar. Even from the surface, off-nadir subglacial returns may systematically prevent successful sounding of the glacier's bed Tober et al. (2024).

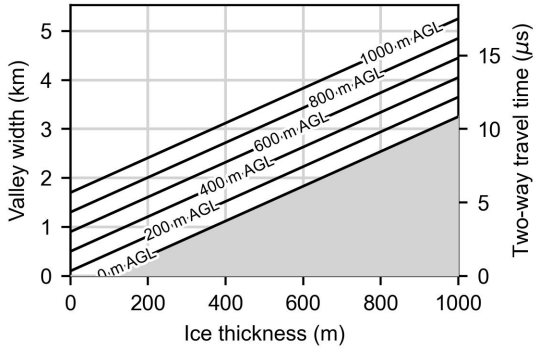

Figure 7. Surface clutter consideration for airborne sounding in valley glaciers. Assuming the aircraft is being flown along the valley's center, for a particular glacier thickness, and glacial valley width, airborne radar sounding should be performed from *below* the flight altitude indicated by the intersecting line so that valley wall returns do not precede and obscure

potential glacier bed returns. The indicated altitudes account for the recommended 1 μs two-way travel time delay buffer between signal sources.

Preflight clutter simulations can further improve radar mapping success by indicating the upper threshold flight altitude for a particular aircraft survey trajectory as a function of local topography and the expected ice thickness. The benefit of such planning has been demonstrated along Logan Glacier, which had proven a difficult radar target throughout much of Operation IceBridge when operating at typical flight altitudes of ~300 m AGL as dictated by laser altimetry mission objectives. However, Logan was successfully sounded in both 2020 and 2021 at flight altitudes $\leq$100 m above the glacier surface (Figure S13).

Although ARES has successfully sounded almost 1500 m of temperate ice within the Bagley Ice Valley, glacier bed echo strengths are significantly reduced beyond depths of ~1 km (Figure S14). Given that the two-way path loss through a kilometer of ice at 2.5 MHz is beyond 50 dB, or a power reduction of $>10^5$, focused synthetic aperture radar processing may help to improve the detection and resolution of returns from these depths by increasing the along-track resolution and processing gain (Leuschen et al., 2000; Peters et al., 2007).

5 Conclusions

Analysis of radar sounding data acquired during NASA's Operation IceBridge between 2013 and 2021 provides the most extensive inventory of glacier thickness measurements in Alaska-Yukon to date. 5,600 linear-km of radar profile measurements were attained over 88 glaciers from interpretation of the 31,700 linear-km of total data acquired. Most of these measurements (over 4,000 linear-km) are from the world's largest nonpolar ice complex (Tana Glacier, Bering Glacier, Malaspina Glacier, and the Bagley Ice Valley). Two troughs cut the bed of the Bering's piedmont lobe, joining to continue ~55 km up-glacier to the Bagley Ice Valley. Bed elevation remains below sea level along the entirety of this trough system. Radar sounding reveals previously obscured tectonic structure of the Saint Elias orogen. Both Malaspina and Bering Glacier have subglacial topography shaped by regional tectonics. The distinct trough observed at the bed of Bering is likely a manifestation of the Bering Fault, which represents the structural boundary at the western limb of the Saint Elias orogen, extending onshore from the Aleutian megathrust.

While interpolation of radar-derived bed elevations to a gridded surface is feasible for Malaspina and Bering Glacier due to dense measurement coverage provided by Operation IceBridge data, ice thickness measurements remain spatially limited for many other glaciers in the region. Observed bed returns for many of the region's glaciers are limited to either the terminus or accumulation areas, distant from high relief topography. Still, these data may prove helpful in constraining modeling efforts (Maffezzoli et al., 2025). The termini of many land- and lake-terminating glaciers are observed to have overdeepened beds, offering insight into the

potential extent of proglacial lakes and associated natural hazards, such as lake outburst floods, given continued glacier retreat.

Long-wavelength airborne radar sounders have proven capable of proving though nearly 1500 m of temperate ice in the Bagley Ice Valley. Though the greatest remaining challenge in sounding Alaskan glaciers is interference caused by high topographic relief, careful survey planning can help mitigate this issue and increase the yield of bed echo retrievals in future campaigns.

Acknowledgements

The authors express their gratitude for Paul Claus and Ultima Thule Outfitters of Alaska for providing the flight services that enabled acquisition of the data presented herein. The Copernicus-30 digital elevation model was acquired from the European Space Agency: https://doi.org/10.5270/ESA-c5d3d65. We thank Sean Gulick for many insightful discussions regarding the connections between subglacial topography and regional tectonic structure of the Saint Elias orogen. BT was funded by NASA's FINESST fellowship program, NASA award 80NSSC19K1357. All authors were supported by Operation IceBridge Alaska, NASA award NNX16AC32G.

Data and Code Availability

Operation IceBridge-Alaska lidar and radar sounding data used in this study are available through the National Snow and Ice Data Center (NSIDC). Laser altimetry data are located at doi: 10.5067/AATE4JJ91EHC. UAFHF processed radar sounding data are located at doi: 10.5067/Q0AVPHN3250H. ARES processed radar sounding data are located at doi: 10.5067/X2H7MP5DBTYP. IceBridge radar-derived bed elevation and ice thickness measurements presented in this study are hosted by the National Snow and Ice Data Center (NSIDC). Measurements from the UAFHF radar sounder (2013-2015) are located at doi:10.5067/225AMW1MQB4O, while those from ARES (2015-2021) are located at doi:10.5067/IW2LCD7YPOV2. Code and additional data presented in this manuscript are hosted by the University of Arizona's Research Data Repository (available upon publication). For data exploration, a downsampled set of radar-derived measurements can be acquired from GitHub and remotely added to Google Earth Desktop (Add->Network Link).

References

Arcone, S. A. (2002). Airborne-radar stratigraphy and electrical structure of temperate firn: Bagley Ice Field, Alaska, U.S.A. *Journal of Glaciology*, *48*(161), 317–334. https://doi.org/10.3189/172756502781831412

Arcone, S. A. (2009). Chapter 12—Glaciers and Ice Sheets. In H. M. Jol (Ed.), *Ground Penetrating Radar Theory and Applications* (pp. 361–392). Elsevier. https://doi.org/10.1016/B978-0-444-53348-7.00012-0

Arendt, A. A., Echelmeyer, K. A., Harrison, W. D., Lingle, C. S., & Valentine, V. B. (2002). Rapid Wastage of Alaska Glaciers and Their Contribution to Rising Sea Level. *Science*, *297*(5580), 382–386. https://doi.org/10.1126/science.1072497

Arendt, A., Luthcke, S., Gardner, A., O'Neel, S., Hill, D., Moholdt, G., & Abdalati, W. (2013). Analysis of a GRACE global mascon solution for Gulf of Alaska glaciers. *Journal of Glaciology*, *59*(217), 913–924. https://doi.org/10.3189/2013JoG12J197

Bahr, D. B., Pfeffer, W. T., & Kaser, G. (2015). A review of volume-area scaling of glaciers. *Reviews of Geophysics*, *53*(1), 95–140. https://doi.org/10.1002/2014RG000470

Bogorodsky, V. V., Bentley, C. R., & Gudmandsen, P. E. (1985). Electromagnetic Wave Propagation in Ice. In V. V. Bogorodsky, C. R. Bentley, & P. E. Gudmandsen (Eds.), *Radioglaciology* (pp. 32–47). Springer Netherlands. https://doi.org/10.1007/978-94-009-5275-1_3

Borthwick, L., Muto, A., & Tinto, K. (2025). Gravity modelling of ice thickness and valley geometry on Taku Glacier (T'aakú Kwáan Sít'i), Alaska. *Journal of Glaciology*, *71*, e13. https://doi.org/10.1017/jog.2024.84

Boyce, E. S., Motyka, R. J., & Truffer, M. (2007). Flotation and retreat of a lake-calving terminus, Mendenhall Glacier, southeast Alaska, USA. *Journal of Glaciology*, *53*(181), 211–224. https://doi.org/10.3189/172756507782202928

Bradford, J. H., & Harper, J. T. (2005). Wave field migration as a tool for estimating spatially continuous radar velocity and water content in glaciers. *Geophysical Research Letters*, *32*(8). https://doi.org/10.1029/2004GL021770

Bruhn, R. L., Forster, R. R., Ford, A. L. J., Pavlis, T. L., & Vorkink, M. (2010). Structural geology and glacier dynamics, Bering and Steller Glaciers, Alaska. In R. A. Shuchman & E. G. Josberger, *Bering Glacier: Interdisciplinary Studies of Earth's Largest Temperate Surging Glacier*. Geological Society of America. https://doi.org/10.1130/2010.2462(11)

Bruhn, R. L., Pavlis, T. L., Plafker, G., & Serpa, L. (2004). Deformation during terrane accretion in the Saint Elias orogen, Alaska. *GSA Bulletin*, *116*(7–8), 771–787. https://doi.org/10.1130/B25182.1

Bruhn, R. L., Sauber, J., Cotton, M. M., Pavlis, T. L., Burgess, E., Ruppert, N., & Forster, R. R. (2012). Plate margin deformation and active tectonics along the northern edge of the Yakutat Terrane in the Saint Elias Orogen, Alaska, and Yukon, Canada. *Geosphere*, *8*(6), 1384–1407. https://doi.org/10.1130/GES00807.1

Carlson, A. E., Kilmer, Z., Ziegler, L. B., Stoner, J. S., Wiles, G. C., Starr, K., Walczak, M. H., Colgan, W., Reyes, A. V., Leydet, D. J., & Hatfield, R. G. (2017). Recent retreat of Columbia Glacier, Alaska: Millennial context. *Geology*, *45*(6), 547–550. https://doi.org/10.1130/G38479.1

Conway, H., Smith, B., Vaswani, P., Matsuoka, K., Rignot, E., & Claus, P. (2009). A low-frequency ice-penetrating radar system adapted for use from an airplane: Test results from Bering and Malaspina Glaciers, Alaska, USA. *Annals of Glaciology*, *50*(51), 93–97. https://doi.org/10.3189/172756409789097487

Enderlin, E. M., Hamilton, G. S., O'Neel, S., Bartholomaus, T. C., Morlighem, M., & Holt, J. W. (2016). An Empirical Approach for Estimating Stress-Coupling Lengths for Marine-Terminating Glaciers. *Frontiers in Earth Science*, *4*. https://doi.org/10.3389/feart.2016.00104

Evans, S. (1965). Dielectric Properties of Ice and Snow–a Review. *Journal of Glaciology*, *5*(42), 773–792. https://doi.org/10.3189/S0022143000018840

Farinotti, D., Huss, M., Fürst, J. J., Landmann, J., Machguth, H., Maussion, F., & Pandit, A. (2019). A consensus estimate for the ice thickness distribution of all glaciers on Earth. *Nature Geoscience*, *12*(3), Article 3. https://doi.org/10.1038/s41561-019-0300-3

Field, H. R., Armstrong, W. H., & Huss, M. (2021). Gulf of Alaska ice-marginal lake area change over the Landsat record and potential physical controls. *The Cryosphere*, *15*(7), 3255–3278. https://doi.org/10.5194/tc-15-3255-2021

Fujita, S., Matsuoka, T., Ishida, T., Matsuoka, K., & Mae, S. (2000). *A summary of the complex dielectric permittivity of ice in the megahertz range and its applications for radar sounding of polar ice sheets*.

Gardner, A. S., Moholdt, G., Cogley, J. G., Wouters, B., Arendt, A. A., Wahr, J., Berthier, E., Hock, R., Pfeffer, W. T., Kaser, G., Ligtenberg, S. R. M., Bolch, T., Sharp, M. J., Hagen, J. O., Broeke, M. R. van den, & Paul, F. (2013). A Reconciled Estimate of Glacier Contributions to Sea Level Rise: 2003 to 2009. *Science*, *340*(6134), 852–857. https://doi.org/10.1126/science.1234532

548 Gogineni, S., Chuah, T., Allen, C., Jezek, K., & Moore, R. K. (1998). An improved coherent radar depth sounder.
549 *Journal of Glaciology*, *44*(148), 659–669. https://doi.org/10.3189/S0022143000002161
550 Harig, C., & Simons, F. J. (2016). Ice mass loss in Greenland, the Gulf of Alaska, and the Canadian Archipelago:
551 Seasonal cycles and decadal trends. *Geophysical Research Letters*, *43*(7), 3150–3159.
552 https://doi.org/10.1002/2016GL067759
553 Harrison, W. D., Raymond, C. F., Echelmeyer, K. A., & Krimmel, R. M. (2003). A macroscopic approach to glacier
554 dynamics. *Journal of Glaciology*, *49*(164), 13–21. https://doi.org/10.3189/172756503781830917
555 Herreid, S., & Pellicciotti, F. (2020). The state of rock debris covering Earth's glaciers. *Nature Geoscience*, *13*(9),
556 Article 9. https://doi.org/10.1038/s41561-020-0615-0
557 Holt, J. W., Peters, M. E., Kempf, S. D., Morse, D. L., & Blankenship, D. D. (2006). Echo source discrimination in
558 single-pass airborne radar sounding data from the Dry Valleys, Antarctica: Implications for orbital
559 sounding of Mars. *Journal of Geophysical Research: Planets*, *111*(E6).
560 https://doi.org/10.1029/2005JE002525
561 Holt, J. W., Truffer, M., Larsen, C. F., Christoffersen, M. S., & Tober, B. S. (2021). *IceBridge ARES L1B*
562 *Geolocated Radar Echo Strength Profiles, version 1* [Dataset]. NASA National Snow and Ice Data Center
563 DAAC. https://doi.org/10.5067/X2H7MP5DBTYP
564 Hugonnet, R., McNabb, R., Berthier, E., Menounos, B., Nuth, C., Girod, L., Farinotti, D., Huss, M., Dussaillant, I.,
565 Brun, F., & Kääb, A. (2021). Accelerated global glacier mass loss in the early twenty-first century. *Nature*,
566 *592*(7856), Article 7856. https://doi.org/10.1038/s41586-021-03436-z
567 Huss, M., & Hock, R. (2018). Global-scale hydrological response to future glacier mass loss. *Nature Climate*
568 *Change*, *8*(2), Article 2. https://doi.org/10.1038/s41558-017-0049-x
569 Jacob, T., Wahr, J., Pfeffer, W. T., & Swenson, S. (2012). Recent contributions of glaciers and ice caps to sea level
570 rise. *Nature*, *482*(7386), 514–518. https://doi.org/10.1038/nature10847
571 Jóhannesson, T., Raymond, C., & Waddington, E. (1989). Time–Scale for Adjustment of Glaciers to Changes in
572 Mass Balance. *Journal of Glaciology*, *35*(121), 355–369. https://doi.org/10.3189/S002214300000928X
573 Kienholz, C., Pierce, J., Hood, E., Amundson, J. M., Wolken, G. J., Jacobs, A., Hart, S., Wikstrom Jones, K., Abdel-
574 Fattah, D., Johnson, C., & Conaway, J. S. (2020). Deglacierization of a Marginal Basin and Implications

for Outburst Floods, Mendenhall Glacier, Alaska. *Frontiers in Earth Science*, *8*. https://www.frontiersin.org/articles/10.3389/feart.2020.00137

Kovacs, A., Gow, A. J., & Morey, R. M. (1995). The in-situ dielectric constant of polar firn revisited. *Cold Regions Science and Technology*, *23*(3), 245–256. https://doi.org/10.1016/0165-232X(94)00016-Q

Lapazaran, J. J., Otero, J., Martín-Español, A., & Navarro, F. J. (2016). On the errors involved in ice-thickness estimates I: Ground-penetrating radar measurement errors. *Journal of Glaciology*, *62*(236), 1008–1020. https://doi.org/10.1017/jog.2016.93

Larsen, C. F., Burgess, E., Arendt, A. A., O'Neel, S., Johnson, A. J., & Kienholz, C. (2015). Surface melt dominates Alaska glacier mass balance. *Geophysical Research Letters*, *42*(14), 5902–5908. https://doi.org/10.1002/2015GL064349

Larsen, C. F., Motyka, R. J., Arendt, A. A., Echelmeyer, K. A., & Geissler, P. E. (2007). Glacier changes in southeast Alaska and northwest British Columbia and contribution to sea level rise. *Journal of Geophysical Research: Earth Surface*, *112*(F1). https://doi.org/10.1029/2006JF000586

Leuschen, C., Gogineni, S., & Tammana, D. (2000). SAR processing of radar echo sounder data. *IGARSS 2000. IEEE 2000 International Geoscience and Remote Sensing Symposium. Taking the Pulse of the Planet: The Role of Remote Sensing in Managing the Environment. Proceedings (Cat. No.00CH37120)*, *6*, 2570–2572 vol.6. https://doi.org/10.1109/IGARSS.2000.859643

Loso, M. G., Larsen, C. F., Tober, B. S., Christoffersen, M., Fahnestock, M., Holt, J. W., & Truffer, M. (2021). Quo vadis, Alsek? Climate-driven glacier retreat may change the course of a major river outlet in southern Alaska. *Geomorphology*, *384*, 107701. https://doi.org/10.1016/j.geomorph.2021.107701

Lützow, N., Higman, B., Truffer, M., Bookhagen, B., Knuth, F., Korup, O., Hughes, K. E., Geertsema, M., Clague, J. J., & Veh, G. (2024). Larger lake outbursts despite glacier thinning at ice-dammed Desolation Lake, Alaska. *EGUsphere*, 1–29. https://doi.org/10.5194/egusphere-2024-2812

MacGregor, J. A., Boisvert, L. N., Medley, B., Petty, A. A., Harbeck, J. P., Bell, R. E., Blair, J. B., Blanchard-Wrigglesworth, E., Buckley, E. M., Christoffersen, M. S., Cochran, J. R., Csathó, B. M., Marco, E. L. D., Dominguez, R. T., Fahnestock, M. A., Farrell, S. L., Gogineni, S. P., Greenbaum, J. S., Hansen, C. M., … Yungel, J. K. (2021). The Scientific Legacy of NASA's Operation IceBridge. *Reviews of Geophysics*, *59*(2), e2020RG000712. https://doi.org/10.1029/2020RG000712

MacGregor, J. A., Winebrenner, D. P., Conway, H., Matsuoka, K., Mayewski, P. A., & Clow, G. D. (2007). Modeling englacial radar attenuation at Siple Dome, West Antarctica, using ice chemistry and temperature data. *Journal of Geophysical Research: Earth Surface*, *112*(F3). https://doi.org/10.1029/2006JF000717

Maffezzoli, N., Rignot, E., Barbante, C., Petersen, T., & Vascon, S. (2025). A gradient-boosted tree framework to model the ice thickness of the world's glaciers (IceBoost v1.1). *Geoscientific Model Development*, *18*(9), 2545–2568. https://doi.org/10.5194/gmd-18-2545-2025

Millan, R., Mouginot, J., Rabatel, A., & Morlighem, M. (2022). Ice velocity and thickness of the world's glaciers. *Nature Geoscience*, *15*(2), Article 2. https://doi.org/10.1038/s41561-021-00885-z

Molnia, B. (2001). *U.S. Geological Survey Professional Paper 1386-K*. https://pubs.usgs.gov/pp/p1386k/

Motyka, R. J., Truffer, M., Kuriger, E. M., & Bucki, A. K. (2006). Rapid erosion of soft sediments by tidewater glacier advance: Taku Glacier, Alaska, USA. *Geophysical Research Letters*, *33*(24). https://doi.org/10.1029/2006GL028467

Otto, J.-C. (2019). Proglacial Lakes in High Mountain Environments. In T. Heckmann & D. Morche (Eds.), *Geomorphology of Proglacial Systems: Landform and Sediment Dynamics in Recently Deglaciated Alpine Landscapes* (pp. 231–247). Springer International Publishing. https://doi.org/10.1007/978-3-319-94184-4_14

Paden, J., Li, J., Leuschen, C., & Rodriguez-Morales, F. (2014). *IceBridge Snow Radar L1B Geolocated Radar Echo Strength Profiles, Version 2* [Dataset]. NASA National Snow and Ice Data Center DAAC. https://doi.org/10.5067/FAZTWP500V70

Peters, M. E., Blankenship, D. D., Carter, S. P., Kempf, S. D., Young, D. A., & Holt, J. W. (2007). Along-Track Focusing of Airborne Radar Sounding Data From West Antarctica for Improving Basal Reflection Analysis and Layer Detection. *IEEE Transactions on Geoscience and Remote Sensing*, *45*(9), 2725–2736. IEEE Transactions on Geoscience and Remote Sensing. https://doi.org/10.1109/TGRS.2007.897416

Pfeffer, W. T., Arendt, A. A., Bliss, A., Bolch, T., Cogley, J. G., Gardner, A. S., Hagen, J.-O., Hock, R., Kaser, G., Kienholz, C., Miles, E. S., Moholdt, G., Mölg, N., Paul, F., Radić, V., Rastner, P., Raup, B. H., Rich, J., Sharp, M. J., & Consortium, T. R. (2014). The Randolph Glacier Inventory: A globally complete inventory of glaciers. *Journal of Glaciology*, *60*(221), 537–552. https://doi.org/10.3189/2014JoG13J176

630 Plafker, G. (1987). *Regional Geology and Petroleum Potential of the Northern Gulf of Alaska Continental Margin*.
631 http://archives.datapages.com/data/circ_pac/0007/0229_f.htm
632 Plaut, J. J., Picardi, G., Safaeinili, A., Ivanov, A. B., Milkovich, S. M., Cicchetti, A., Kofman, W., Mouginot, J.,
633 Farrell, W. M., Phillips, R. J., Clifford, S. M., Frigeri, A., Orosei, R., Federico, C., Williams, I. P., Gurnett,
634 D. A., Nielsen, E., Hagfors, T., Heggy, E., … Edenhofer, P. (2007). Subsurface Radar Sounding of the
635 South Polar Layered Deposits of Mars. *Science*, *316*(5821), 92–95.
636 https://doi.org/10.1126/science.1139672
637 Post, A. (1969). Distribution of Surging Glaciers in Western North America. *Journal of Glaciology*, *8*(53), 229–240.
638 https://doi.org/10.3189/S0022143000031221
639 Post, A., O'Neel, S., Motyka, R. J., & Streveler, G. (2011). A complex relationship between calving glaciers and
640 climate. *Eos, Transactions American Geophysical Union*, *92*(37), 305–306.
641 https://doi.org/10.1029/2011EO370001
642 Rasmussen, C. E., & Williams, C. K. (2006). *Gaussian processes for machine learning. Number ISBN 0-262-18253-*
643 *X*. The MIT Press. www.GaussianProcess.org/gpml
644 RGI Consortium. (2017). *Randolph Glacier Inventory—A Dataset of Global Glacier Outlines, Version 6* [Dataset].
645 NASA National Snow and Ice Data Center DAAC. https://doi.org/10.7265/4m1f-gd79
646 Rignot, E., Mouginot, J., Larsen, C. F., Gim, Y., & Kirchner, D. (2013). Low-frequency radar sounding of temperate
647 ice masses in Southern Alaska. *Geophysical Research Letters*, *40*(20), 5399–5405.
648 https://doi.org/10.1002/2013GL057452
649 Rodriguez-Morales, F., Gogineni, S., Leuschen, C. J., Paden, J. D., Li, J., Lewis, C. C., Panzer, B., Gomez-Garcia
650 Alvestegui, D., Patel, A., Byers, K., Crowe, R., Player, K., Hale, R. D., Arnold, E. J., Smith, L., Gifford, C.
651 M., Braaten, D., & Panton, C. (2014). Advanced Multifrequency Radar Instrumentation for Polar Research.
652 *IEEE Transactions on Geoscience and Remote Sensing*, *52*(5), 2824–2842. IEEE Transactions on
653 Geoscience and Remote Sensing. https://doi.org/10.1109/TGRS.2013.2266415
654 Rounce, D. R., Hock, R., Maussion, F., Hugonnet, R., Kochtitzky, W., Huss, M., Berthier, E., Brinkerhoff, D.,
655 Compagno, L., Copland, L., Farinotti, D., Menounos, B., & McNabb, R. W. (2023). Global glacier change
656 in the 21st century: Every increase in temperature matters. *Science*, *379*(6627), 78–83.
657 https://doi.org/10.1126/science.abo1324

Scherler, D., Wulf, H., & Gorelick, N. (2018). Global Assessment of Supraglacial Debris-Cover Extents. *Geophysical Research Letters*, *45*(21), 11,798-11,805. https://doi.org/10.1029/2018GL080158

Sheriff, R. E. (1980). Nomogram for Fresnel-zone calculation. *Geophysics*, *45*(5), 968–972. https://doi.org/10.1190/1.1441101

Shugar, D. H., Clague, J. J., Best, J. L., Schoof, C., Willis, M. J., Copland, L., & Roe, G. H. (2017). River piracy and drainage basin reorganization led by climate-driven glacier retreat. *Nature Geoscience*, *10*(5), Article 5. https://doi.org/10.1038/ngeo2932

Smith, B. M. E., & Evans, S. (1972). Radio Echo Sounding: Absorption and Scattering by Water Inclusion and Ice Lenses. *Journal of Glaciology*, *11*(61), 133–146. https://doi.org/10.3189/S0022143000022541

Tober, B. S., & Christoffersen, M. S. (2020). *Radar Analysis Graphical Utility (RAGU)* [Software]. Zenodo. https://doi.org/10.5281/zenodo.3968981

Tober, B. S., Christoffersen, M. S., Holt, J. W., Truffer, M., & Larsen, C. F. (2024). Thickness of Ruth Glacier, Alaska, and depth of its Great Gorge from ice-penetrating radar and mass conservation. *Journal of Glaciology*, 1–10. https://doi.org/10.1017/jog.2024.53

Tober, B. S., Holt, J. W., Christoffersen, M. S., Truffer, M., Larsen, C. F., Brinkerhoff, D. J., & Mooneyham, S. A. (2023). Comprehensive Radar Mapping of Malaspina Glacier (Sít' Tlein), Alaska—The World's Largest Piedmont Glacier—Reveals Potential for Instability. *Journal of Geophysical Research: Earth Surface*, *128*(3), e2022JF006898. https://doi.org/10.1029/2022JF006898

Truffer, M., & Motyka, R. J. (2016). Where glaciers meet water: Subaqueous melt and its relevance to glaciers in various settings. *Reviews of Geophysics*, *54*(1), 220–239. https://doi.org/10.1002/2015RG000494

Truffer, Martin, Holt, John, Larsen, Christopher, Christoffersen, Michael, & B. S. Tober. (2021). *IceBridge UAF L1B HF Geolocated Radar Echo Strength Profiles, version 1* [Dataset]. NASA National Snow and Ice Data Center DAAC. https://doi.org/10.5067/Q0AVPHN3250H

Trüssel, B. L., Truffer, M., Hock, R., Motyka, R. J., Huss, M., & Zhang, J. (2015). Runaway thinning of the low-elevation Yakutat Glacier, Alaska, and its sensitivity to climate change. *Journal of Glaciology*, *61*(225), 65–75. https://doi.org/10.3189/2015JoG14J125

Watts, R. D., & England, A. W. (1976). Radio-echo Sounding of Temperate Glaciers: Ice Properties and Sounder Design Criteria. *Journal of Glaciology*, *17*(75), 39–48. https://doi.org/10.3189/S0022143000030707

686 Welty, E., Zemp, M., Navarro, F., Huss, M., Fürst, J. J., Gärtner-Roer, I., Landmann, J., Machguth, H., Naegeli, K.,
687 Andreassen, L. M., Farinotti, D., Li, H., & GlaThiDa Contributors. (2020). Worldwide version-controlled
688 database of glacier thickness observations. *Earth System Science Data*, *12*(4), 3039–3055.
689 https://doi.org/10.5194/essd-12-3039-2020
690 Windnagel, A., Hock, R., Maussion, F., Paul, F., Rastner, P., Raup, B., & Zemp, M. (2022). Which glaciers are the
691 largest in the world? *Journal of Glaciology*, 1–10. https://doi.org/10.1017/jog.2022.61
692 Young, E. M., Flowers, G. E., Berthier, E., & Latto, R. (2021). An imbalancing act: The delayed dynamic response
693 of the Kaskawulsh Glacier to sustained mass loss. *Journal of Glaciology*, *67*(262), 313–330.
694 https://doi.org/10.1017/jog.2020.107
695 Zemp, M., Huss, M., Thibert, E., Eckert, N., McNabb, R., Huber, J., Barandun, M., Machguth, H., Nussbaumer, S.
696 U., Gärtner-Roer, I., Thomson, L., Paul, F., Maussion, F., Kutuzov, S., & Cogley, J. G. (2019). Global
697 glacier mass changes and their contributions to sea-level rise from 1961 to 2016. *Nature*, *568*(7752),
698 Article 7752. https://doi.org/10.1038/s41586-019-1071-0
699

Journal of Geophysical Research: Earth Surface

Supporting Information for

Alaskan Glacier Depths from a Decade of Airborne Radar Sounding

B. S. Tober[1,2], M. S. Christoffersen[3,4], J. W. Holt[1,4], M. Truffer[5,6], and C. F. Larsen[5]

[1]Dept. of Geosciences, University of Arizona, Tucson, AZ, USA

[2]Civil and Environmental Engineering, Carnegie Mellon University, Pittsburgh, PA, USA

[3]School of Earth and Atmospheric Sciences, Georgia Institute of Technology, Atlanta, GA, USA

[4]Lunar and Planetary Laboratory, University of Arizona, Tucson, AZ, USA

[5]Geophysical Institute, University of Alaska Fairbanks, Fairbanks, AK, USA

[6]Dept. of Physics, University of Alaska Fairbanks, Fairbanks, AK, USA

Corresponding author: Brandon S. Tober (btober@cmu.edu)

Contents of this file

Additional Supporting Information (Files uploaded separately)

Text S1.

The separation distance between plane waves returned to the radar sounder dictates whether they will add together constructively or destructively. Waves which are returned within distances that are half an even multiple of the wavelength $\left(\frac{2n\lambda}{2}, n \in Z\right)$, where λ is the radar wavelength, will add together constructively (Sheriff, 1980). The first area ($n = 0$) from which plane waves will return to the radar constructively is known as the first Fresnel zone. For $n > 0$, successive Fresnel zones form concentric rings. We estimate the centroid location from which surface reflections originate as the area of the first Fresnel zone, representing the horizontal resolution at the surface. Plane waves which return to the radar from the glacier surface within a distance of $\lambda/2$ will have reached the glacier surface within a distance of $\lambda/4$, thus traveling a maximum one-way distance of up to $z + \lambda/4$, where z is the aircraft height above the surface. Solving for the radius of the first Fresnel zone at the surface r_f given the aircraft height z and the hypotenuse $z + \lambda/4$, we find:

$$z \leq \frac{v_1}{2}\left(\frac{w}{v_1} - \frac{2h}{v_2} - 1\,\mu s\right) \tag{1}$$

Text S2.

As with the first Fresnel zone at the glacier's surface (Text S1), the horizontal resolution of radar returns at the bed of the glacier can be assessed by considering the near-nadir area from which waves return to the sounder within one-half a wavelength. However, as waves cross the air-ice interface, we must consider refraction and a change in wavespeed. The path length of a plane wave in air l_1 increases with the aircraft's height above the surface z and the takeoff angle θ_1:

$$l_1 = \sqrt{z^2 + (z\ tan\ tan\ \theta_1\ )^2} \tag{2}$$

At the air-ice boundary, plane waves are refracted at an angle θ_2 given by Snell's Law as:

$$\theta_2 = sin^{-1}(\ sin\ (\theta_1)\ \ \frac{v_2}{v_1}\ ) \tag{3}$$

where v_1 is the radar wavespeed in air (assumed to be a vacuum), and v_2 is the radar wavespeed in ice. The path length l_2 in ice of thickness h follows Equations (2, 3):

$$l_2\ = \sqrt{h^2 + (h\ tan\ tan\ \theta_2\ )^2} \tag{4}$$

The total two-way travel time of plane waves through this two-layer half space follows as:

$$ztwtt = (2l_1)/v_1 + (2l_2)/v_2 \tag{5}$$

The number of wave cycles completed over this distance is then calculated by multiplying the two-way travel time by the radar frequency.

Assuming a wavespeed in ice of 169 m μs^{-1}, for a given aircraft height z and ice thickness h, we numerically determined the greatest takeoff angle $\theta_{1_{max}}$ such that off-nadir plane waves ($\theta_1 > 0°$) have a two-way path distance difference of less than half a wavelength (within half a cycle) from that of the nadir path ($\theta_1 = 0°$). The angle of refraction $\theta_{2_{max}}$ associated with this maximum takeoff angle is found by setting $\theta_1 = \theta_{1_{max}}$ in Equation (3).

The horizontal resolution at the glacier bed r_f' is then represented by the radius at the bed given by takeoff angle $\theta_{1_{max}}$ refraction angle $\theta_{2_{max}}$, the aircraft's height z, and ice thickness h:

$$r_f' = ztan\theta_{1_{max}} + htan\theta_{2_{max}} \tag{6}$$

Text S3.

Assuming that an airborne radar system is being flown along the center of a glacier valley with width w, or at a distance of $\frac{w}{2}$ from an adjacent valley wall, the two-way travel time delay for off-nadir surface returns from the valley walls $twtt_{clutter}$ is:

$$ztwtt_{clutter} = \frac{w}{v_1} \tag{7}$$

where v_1 is the radio wavespeed in air (assumed to be a vacuum).

Similarly, the two-way travel time delay to the bed of a glacier $twtt_{bed}$ of thickness h, from a flight altitude above the glacier surface z is:

$$twtt_{bed} = \frac{2z}{v_1} + \frac{2h}{v_2} \tag{8}$$

where v_2 is the radio wavespeed in ice.

The recommended flight altitude such that potential glacier bed returns will precede off-nadir surface returns by at least 1 μs can be determined by combining Equations (7, 8) through an equality:

$$\frac{2z}{v_1} + \frac{2h}{v_2} \leq \frac{w}{v_1} - 1\ \mu s \tag{9}$$

Rearranging to solve for z, we arrive at:

$$z \leq \frac{v_1}{2}\left(\frac{w}{v_1} - \frac{2h}{v_2} - 1\ \mu s\right) \tag{10}$$

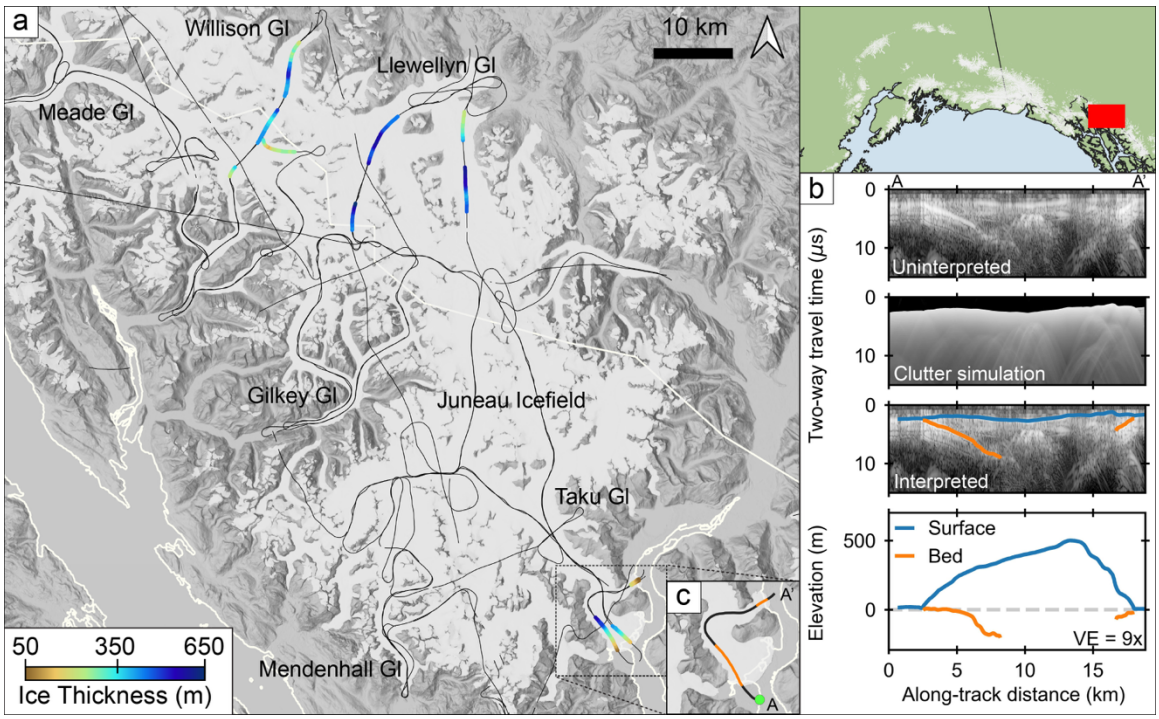

Figure S1. IceBridge radar-derived ice thickness measurements across the Juneau Icefield. (a) Ice thickness measurements atop IceBridge flight tracks (black lines). (b) Example ARES profile over the terminus of Taku Glacier. (c) Map view location of profile shown in panel (b), with along-track locations of bed detections shown in orange.

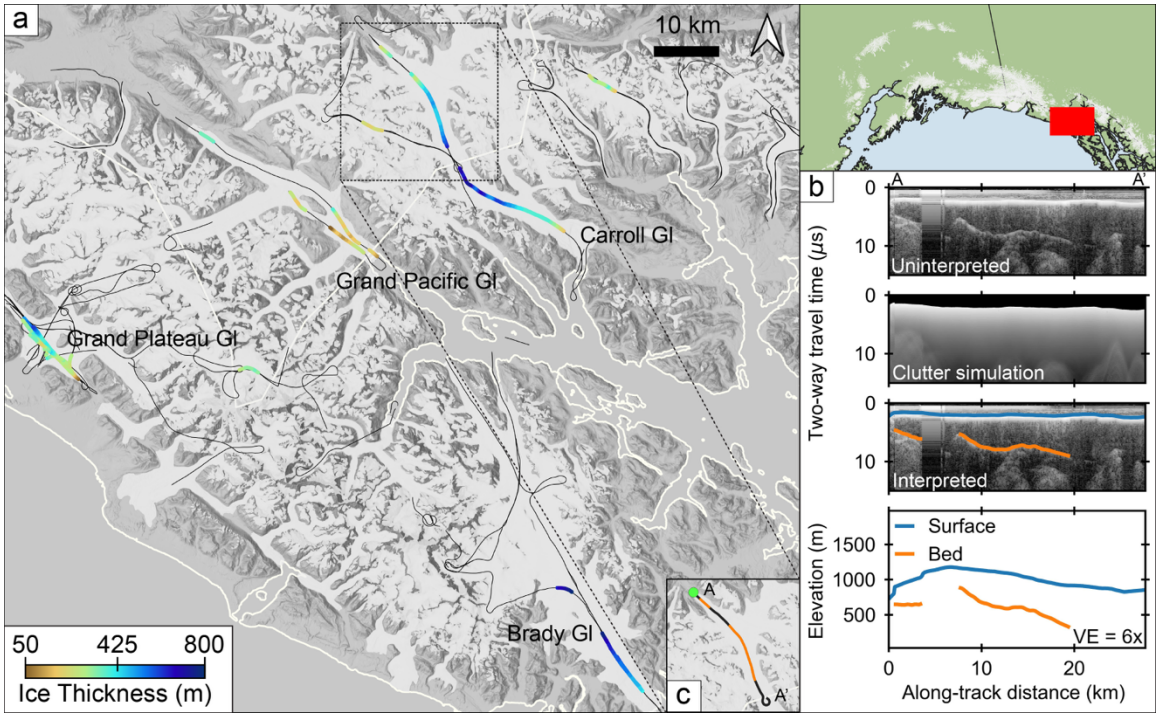

Figure S2. IceBridge radar-derived ice thickness measurements around Glacier Bay. (a) Ice thickness measurements atop IceBridge flight tracks (black lines). (b) Example UAFHF profile over the terminus of Carroll Glacier. (c) Map view location of profile shown in panel (b), with along-track locations of bed detections shown in orange.

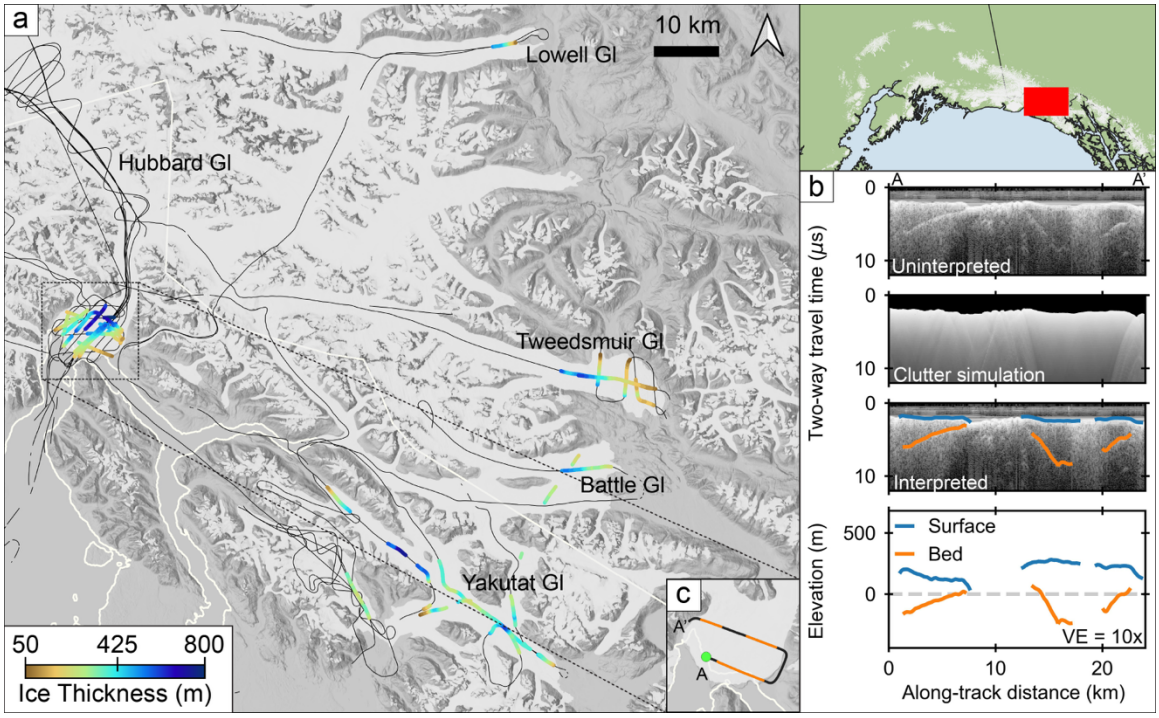

Figure S3. IceBridge radar-derived ice thickness measurements in southeast Alaska. (a) Ice thickness measurements atop IceBridge flight tracks (black lines). (b) Example UAFHF profile over the terminus of Hubbard Glacier. (c) Map view location of profile shown in panel (b), with along-track locations of bed detections shown in orange.

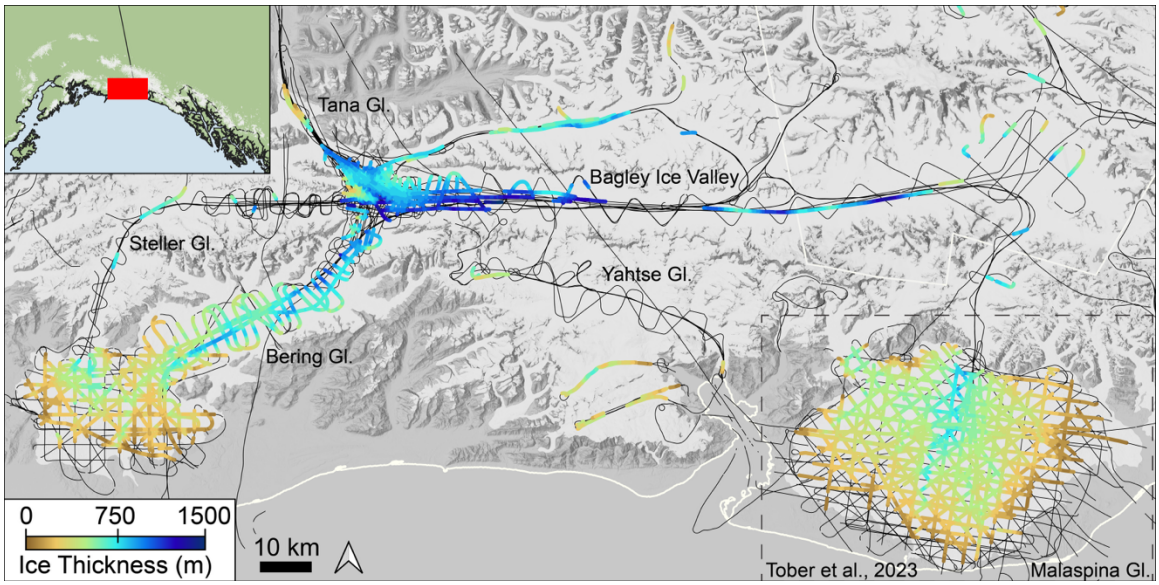

Figure S4. IceBridge radar-derived ice thickness measurements across the Saint Elias Ice Complex atop IceBridge flight tracks (black lines).

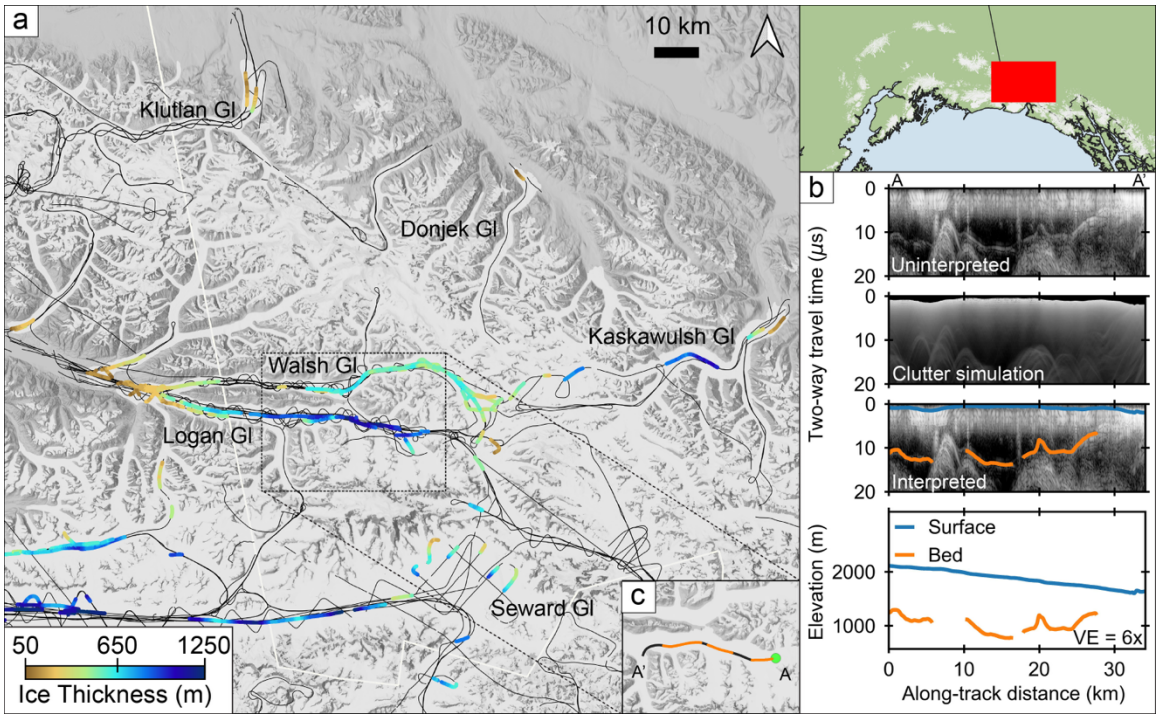

Figure S5. IceBridge radar-derived ice thickness measurements in southwestern Yukon, Canada. (a) Ice thickness measurements atop IceBridge flight tracks (black lines). (b) Example ARES profile over Logan Glacier. (c) Map view location of profile shown in panel (b), with along-track locations of bed detections shown in orange.

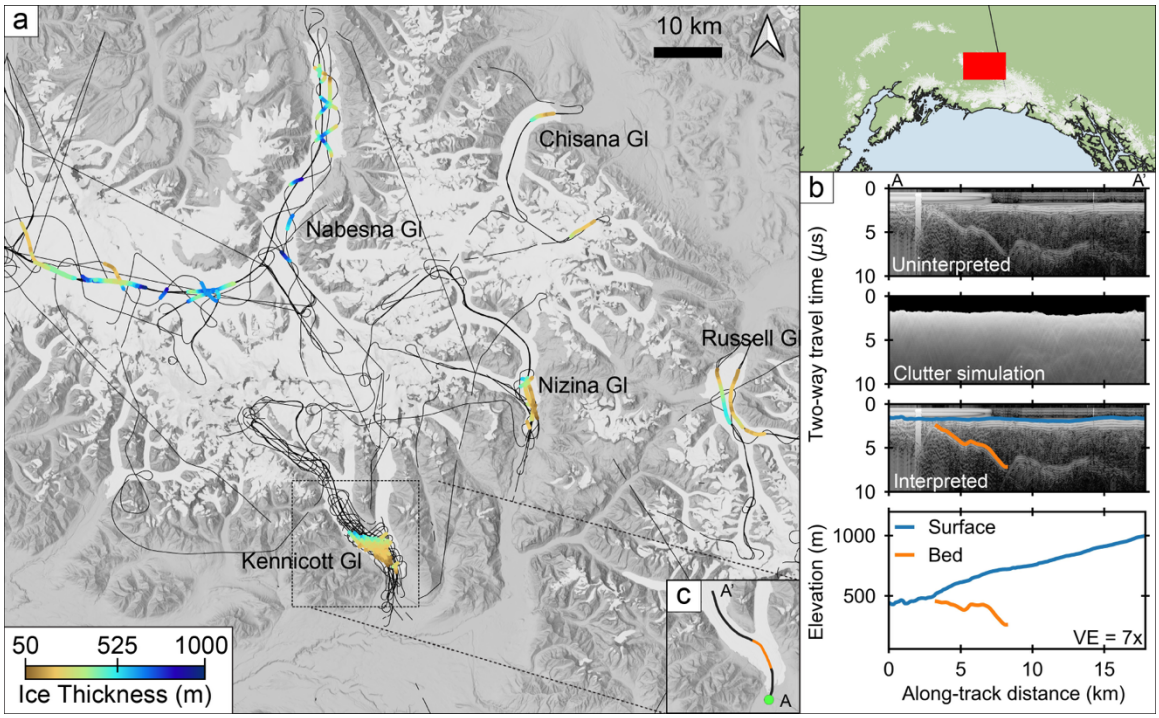

Figure S6. IceBridge radar-derived ice thickness measurements across the Wrangell Mountains. (a) Ice thickness measurements atop IceBridge flight tracks (black lines). (b) Example UAFHF profile over Kennicott Glacier. (c) Map view location of profile shown in panel (b), with along-track locations of bed detections shown in orange.

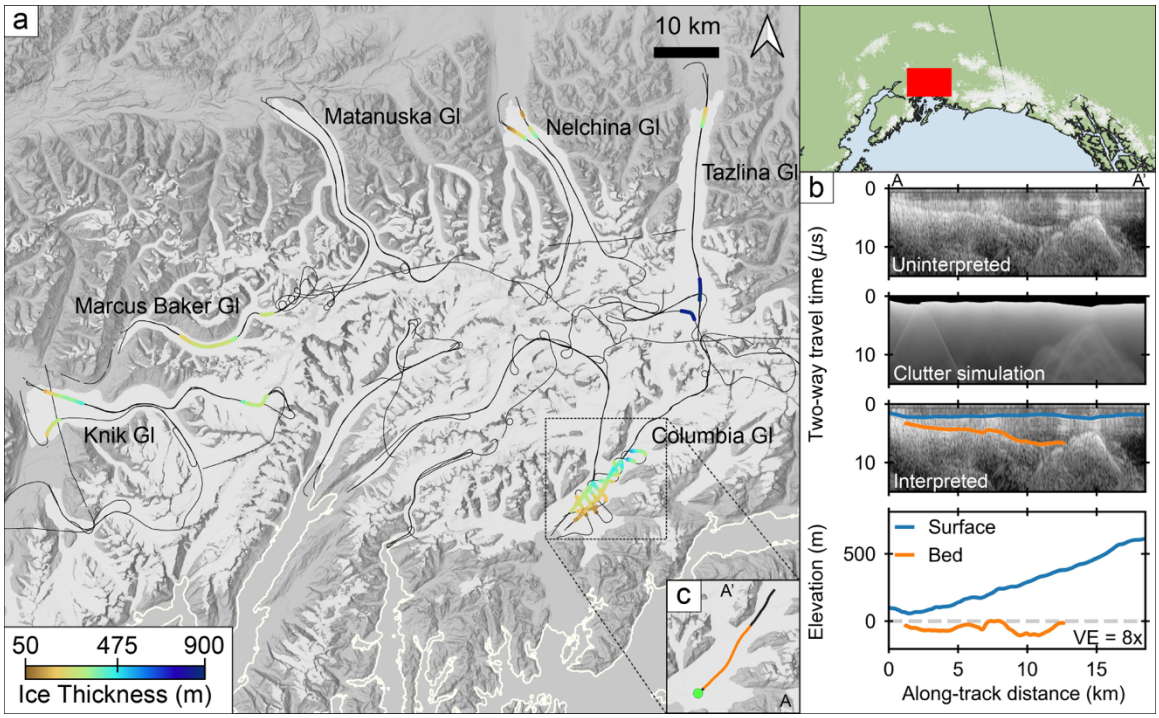

Figure S7. IceBridge radar-derived ice thickness measurements across part of south-central Alaska. (a) Ice thickness measurements atop IceBridge flight tracks (black lines). (b) Example ARES profile over Columbia Glacier. (c) Map view location of profile shown in panel (b), with along-track locations of bed detections shown in orange.

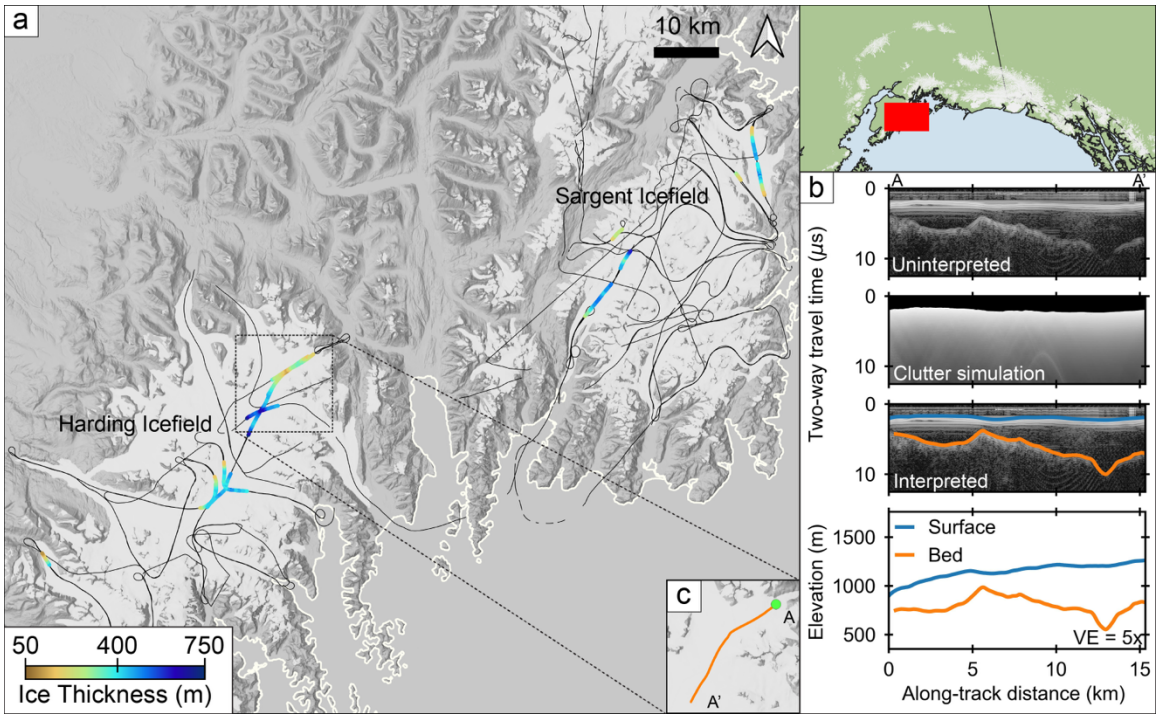

Figure S8. IceBridge radar-derived ice thickness measurements across Sargent and Harding Icefields. (a) Ice thickness measurements atop IceBridge flight tracks (black lines). (b) Example UAFHF profile over Exit Glacier. (c) Map view location of profile shown in panel (b), with along-track locations of bed detections shown in orange.

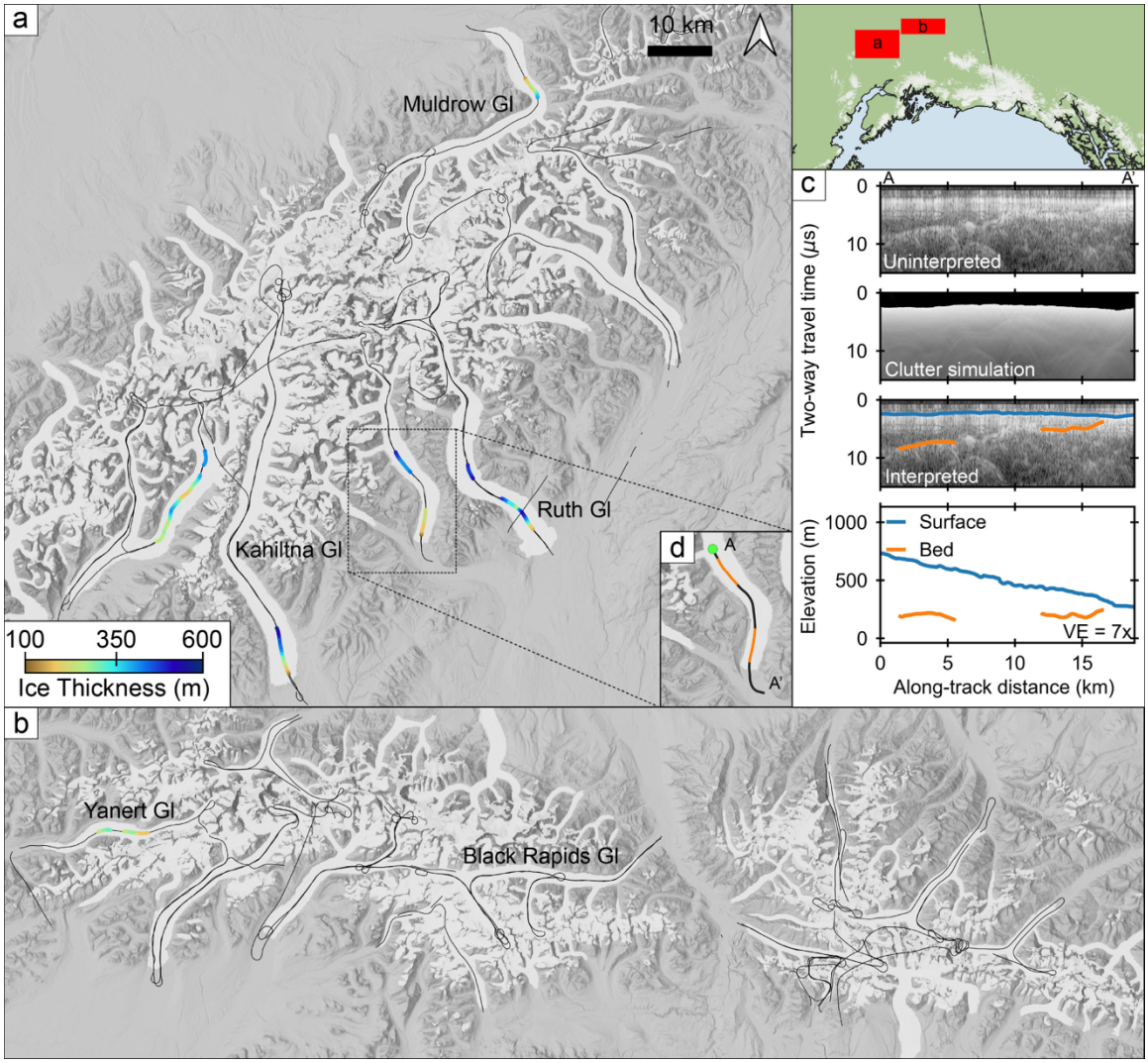

Figure S9. IceBridge radar-derived ice thickness measurements across the Alaska Range. Ice thickness measurements atop IceBridge flight tracks (black lines) for (a) the western Alaska Range, and (b) the eastern Alaska Range. (c) Example ARES profile over Tokositna Glacier. (d) Map view location of profile shown in panel (c), with along-track locations of bed detections shown in orange.

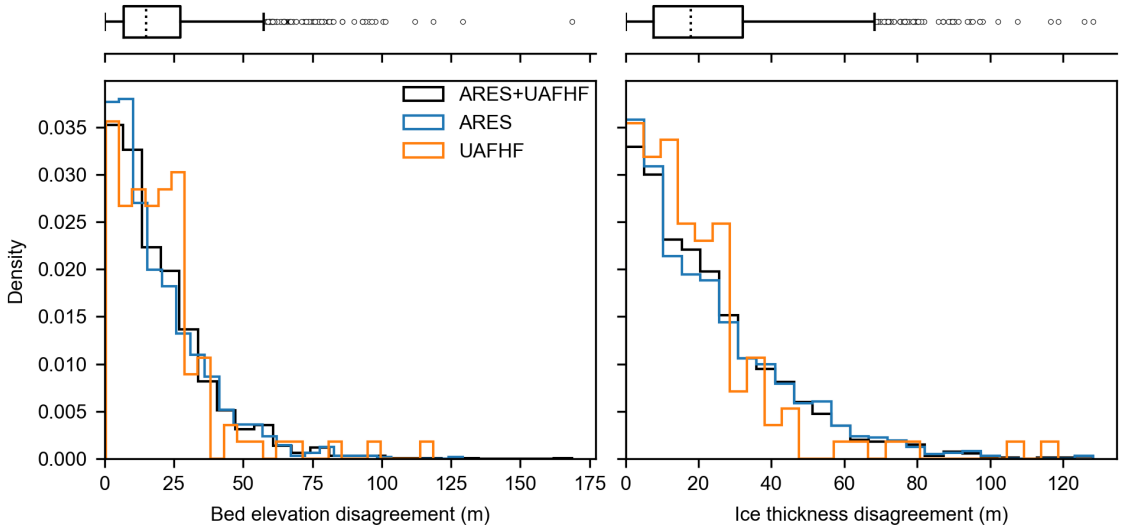

Figure S10. Crossover analysis for IceBridge radar-derived measurements of bed elevation (left) and ice thickness (right). Blue bars represent crossings only between ARES profiles, orange bars represent crossings only between UAFHF profiles, and black bars along with upper boxplots represent all crossings.

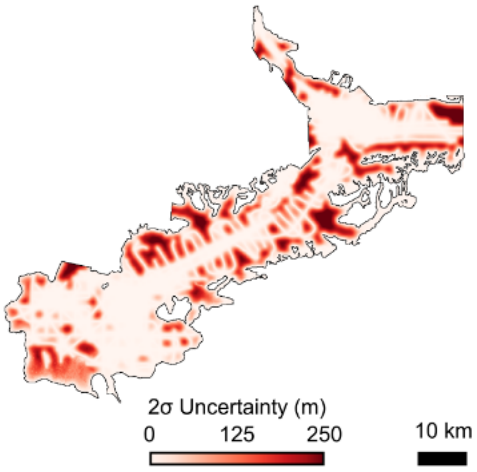

Figure S11. Modeled bed elevation uncertainty across the Bering Glacier System, including the main branch of Tana Glacier and the central Bagley Ice Valley. Uncertainty is represented by twice the marginal standard deviation achieved through Gaussian Process regression.

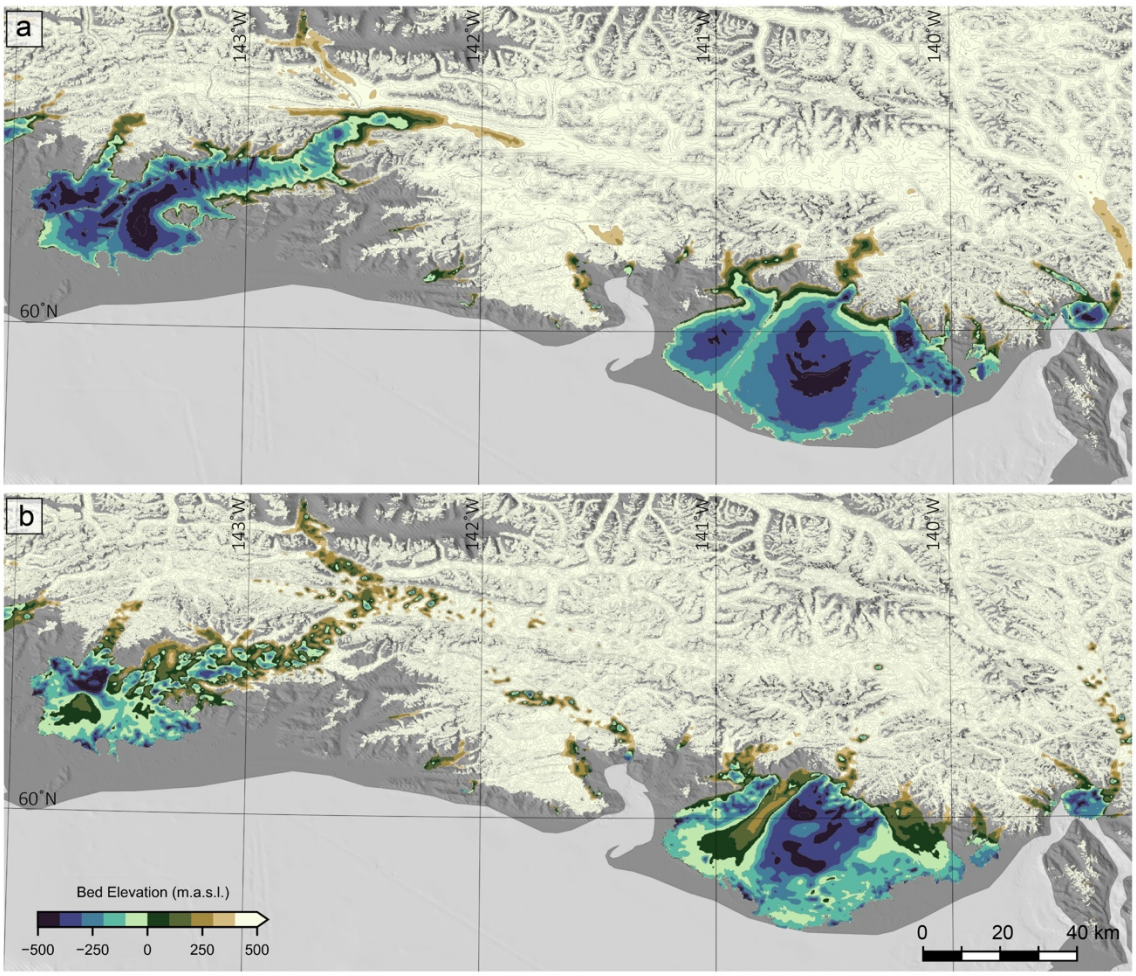

Figure S12. Bed elevations across the Saint Elias Ice Complex for both Farinotti et al. (2019; a) and Millan et al. (2022; b) attained by subtracting the ice thicknesses presented in each of those studies from the 2011 Copernicus 30 digital elevation model. 100 m contour lines for both (a) and (b). Elevations are shown by saturated colors beyond 500 m to emphasize the differences in subglacial morphology for Bering Glacier and Malaspina between these studies and that mapped by Operation IceBridge radar sounding.

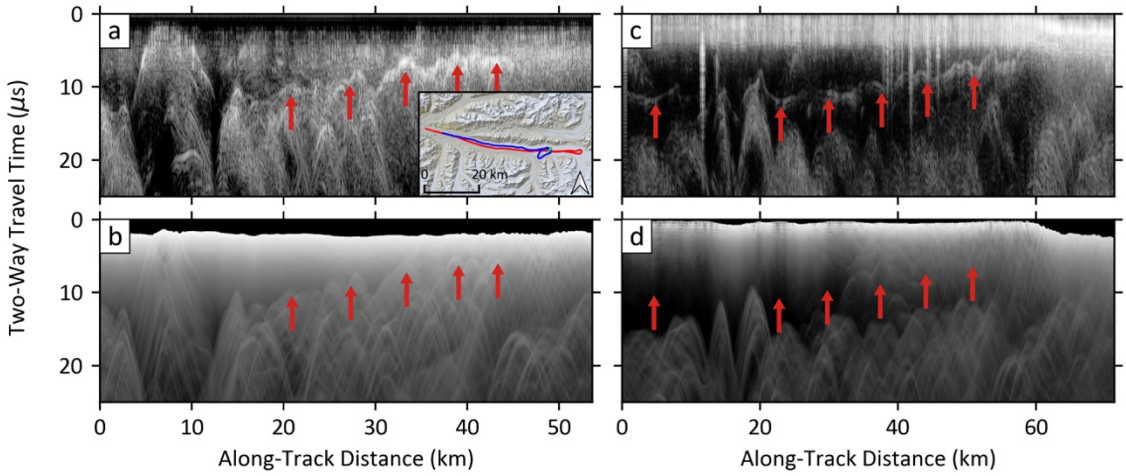

Figure S13. Comparison of radar sounding profiles over Logan Glacier at different flight altitudes. (a) ARES profile and (b) corresponding clutter simulation acquired in 2018 at 300-400 m altitude above ground level. (d) ARES profile and (b) corresponding clutter simulation acquired in 2021 at ~100 m altitude above ground level. The 2018 flight path is shown by the blue line in panel (a) inset map, while the 2021 flight path is shown by the red line, both starting to the east. Surface clutter obscures any potential bed returns in the 2018 profile, while a clear bed return is mapped in 2021 from a lower flight altitude.

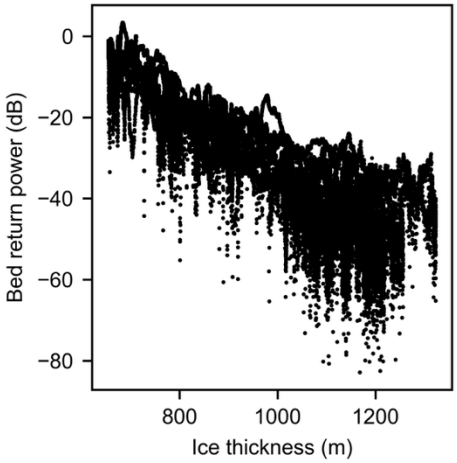

Figure S14. Radar bed return power as a function of ice thickness for an ARES profile along the Bagley Ice Valley.

Table S1. List of 86 Glaciers surveyed by IceBridge between 2013 and 2021 for which >= 1 linear-km was mapped using radar sounding. Separated by Randolph Glacier Inventory version 6 identifier (RGIId), in descending order of the total distance that was mapped. Glacier names and areas from (RGI Consortium, 2017).

RGIId	Area (km^2)	Name	Distance Flown (km)	Distance Mapped (km)
RGI60-01.13696	3363	Seward	3162	1660
RGI60-01.13635	3025	Bering	3909	1140
RGI60-01.23649	832	Agassiz	778	366
RGI60-01.13538	515	Tana	1021	313
RGI60-01.14883	744	Steller	605	214
RGI60-01.27108	534		462	163
RGI60-01.26738	718	Walsh	1044	155
RGI60-01.14443	2834	Hubbard	1346	138
RGI60-01.15769	1029	Nabesna	1065	125
RGI60-01.17566	1177	Logan	875	125
RGI60-01.15645	293	Kennicott	728	92
RGI60-01.23641	488		508	71
RGI60-01.23653	445	Marvine/Hayden	230	70
RGI60-01.10689	774	Columbia	423	67
RGI60-01.21014	458	Carroll	165	57
RGI60-01.16121	592	Tweedsmuir	107	42
RGI60-01.20985	237	Grand Plateau	189	40
RGI60-01.14878	284	Guyot	80	38
RGI60-01.23642	179	Tsaa	97	36
RGI60-01.17348	362	Russell	308	32
RGI60-01.13531	421	Miles	302	29
RGI60-01.16201	1054	Kaskawulsh	325	28
RGI60-01.12645	238	East Yakutat	60	28
RGI60-01.13790	207	Novatak	59	28
RGI60-01.15682	304	Nizina	304	26
RGI60-01.17614	925	Chitina	166	24
RGI60-01.17183	959	Klutlan	696	23
RGI60-01.26736	345	Valerie	132	21
RGI60-01.01513	82	Willison	41	20
RGI60-01.10333	162	Marcus Baker	100	20
RGI60-01.14683	1019	Yahtse	530	20
RGI60-01.20796	549	Brady	176	20
RGI60-01.17807	142	Aialik	87	17
RGI60-01.01522	298	Llewellyn	137	17
RGI60-01.26732	182	Grand Pacific	37	16
RGI60-01.26743	176	Lacuna	84	15
RGI60-01.15135	66		64	14
RGI60-01.01390	521	Taku	282	14
RGI60-01.10196	427	Knik	220	14

RGI60-01.17803	198	Bear	68	14
RGI60-01.17782	98	Harris	41	13
RGI60-01.15788	283	Chisana	121	12
RGI60-01.18087	37	Exit	36	12
RGI60-01.22178	336	Ruth	206	12
RGI60-01.10778	373	Tazlina	293	11
RGI60-01.09211	115	Ellsworth	125	10
RGI60-01.01731	168	Woodworth	36	10
RGI60-01.13838	200	Vern Ritchie	42	10
RGI60-01.17423	512	Barnard	201	9
RGI60-01.23655	183		132	9
RGI60-01.22186	204	Tokositna	75	8
RGI60-01.10683	238	Nelchina	159	8
RGI60-01.09951	46	Princeton	45	8
RGI60-01.23646	140	West Yakutat	144	8
RGI60-01.22193	480	Kahiltna	225	8
RGI60-01.01796	189	Allen	33	7
RGI60-01.01524	461	Meade	212	7
RGI60-01.23563	18	Ultramarine	11	6
RGI60-01.00042	84	Yanert	35	6
RGI60-01.01520	193	Field	182	6
RGI60-01.16545	583	Lowell	77	5
RGI60-01.13789	80	West Nunatak	47	5
RGI60-01.21001	115	Riggs	46	5
RGI60-01.21008	176	Ferris	11	4
RGI60-01.13601	119	Watson	6	4
RGI60-01.22169	332	Muldrow	110	4
RGI60-01.27103	87		27	4
RGI60-01.26721	97	Regal	124	3
RGI60-01.13591	27	White River	7	3
RGI60-01.23565	46	Nellie Juan	53	3
RGI60-01.17761	308	Tustumena	167	3
RGI60-01.15771	169	Copper	216	3
RGI60-01.13826	178	Battle	28	3
RGI60-01.17840	97	Holgate	80	3
RGI60-01.23564	9		5	3
RGI60-01.27102	102	Hole-in-the-Wall	48	3
RGI60-01.16342	448	Donjek	50	3
RGI60-01.21011	247	Melbern	36	2
RGI60-01.14479	219		10	2

RGI60-01.26729	54	Tkope	17	2
RGI60-01.03470	28	Pendant	18	2
RGI60-01.17915	56	Chernof	36	2
RGI60-01.09251	19		34	2
RGI60-01.01741	141	Scott	48	2
RGI60-01.20891	158	Margerie	31	2
RGI60-01.01743	45	Sherman	18	1